CHAPTER 4. FEEDFORWARD ACTIVE CONTROL OF FLEXURAL VIBRATION IN A CYLINDER USING PIEZOCERAMIC ACTUATORS AND AN ANGLE STIFFENER

4.1 INTRODUCTION

In this chapter, the active control of flexural vibration in cylindrical shells using as control sources piezoceramic actuators placed between the flange of a ring stiffener and the shell surface is investigated. The classical equations of motion for the vibration of a shell developed by Flügge (1960) are used to develop a theoretical model for the shell with primary point sources and a ring stiffener and control actuators (Section 4.2).

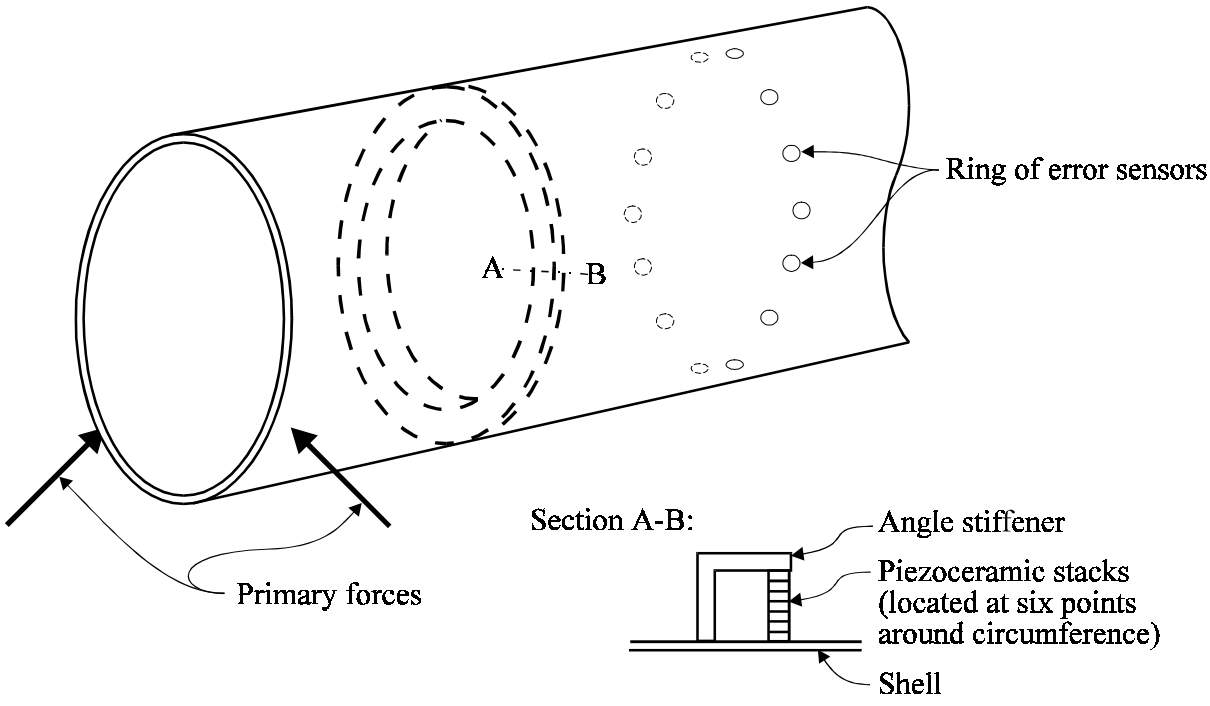

Figure 4.1 Cylinder showing primary sources, ring stiffener, piezoceramic stack control actuators and error sensors.

The effective control signal is a combination of the effects of the point forces at the base of the actuators, and the reaction line force and line moment in a ring at the base of the stiffener (Section 4.2.6). The displacement at a point is the sum of the displacements due to each of the primary source and control source forces and moments. Optimal control is achieved by minimising the total mean square displacement at the location of the ring of error sensors downstream of the control sources.

The theoretical analysis considers two different sets of cylinder supports. In both cases, the left hand end is modelled as free. In the first case, the right hand end is modelled as infinite and in the second the right hand end is modelled as free. The influence of the control source locations, the location of the ring of error sensors and the excitation frequency on the control source amplitude and achievable attenuation are investigated, and the physical reasons for each observation are explained (Section 4.3).

A modal analysis of the cylinder is performed to show that the ring stiffener significantly affects the vibration response of the cylinder. Experimental verification of the theoretical model is performed for the simply supported cylinder with and without active vibration control. The experimental methods are described in Section 4.4. Experimental results are compared with theoretical predictions for the vibration of the cylinder with and without active vibration control (Section 4.5).

4.2 THEORY

4.2.1 The differential equations of motion for a cylindrical shell and the general solution

The differential equations governing the vibration of a cylindrical shell are different from the equations of motion for beams and plates, for two main reasons. First, unlike the cases of the equations of motion for beams and plates, there is no universally accepted version of the equations of motion for the vibration of a cylindrical shell, and second, rather than there being one equation for the transverse vibration of a beam or plate, there are three simultaneous equations to be considered for the coupled vibrations in the radial, axial and tangential directions.

Because of the complex nature of the derivation of the equations of motion from stress-strain relationships, different researchers have derived slightly different equations of motion for shells. Leissa (1973*a*) lists and describes the derivation of the main theories. The simplest form was given by Donnell-Mushtari, and other versions include a variety of complicating terms. Perhaps the most popular version was that developed by Flügge (1960), but including inertia terms (see Section 1.2.1.4).

The response of the cylindrical shell shown in Figure 4.2 to simple harmonic excitations $q_x e^{j\omega t}$, $q_\theta e^{j\omega t}$ and $q_r e^{j\omega t}$ in the axial (x), tangential (θ) and radial (r) directions respectively is considered. The end of the cylinder at $x = 0$ is modelled as simply supported.

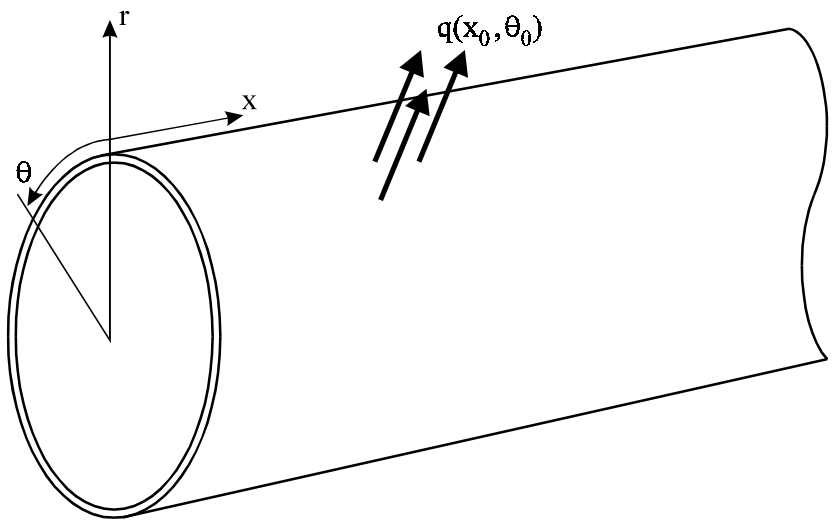

Figure 4.2 Cylinder with excitation q at location (x_0,θ_0).

Following the sign conventions given in Figure 4.3, the Flügge equations of motion for the response of the cylindrical shell shown in Figure 4.2 are

$$R^2\frac{\partial^2 u}{\partial x^2}+\frac{(1-\nu)}{2}\frac{\partial^2 u}{\partial\theta^2}-\frac{\rho R^2(1-\nu^2)}{E}\frac{\partial^2 u}{\partial t^2}+\frac{R(1+\nu)}{2}\frac{\partial^2 v}{\partial x\partial\theta}+R\nu\frac{\partial w}{\partial x}+\left(\frac{(1-\nu)}{2}\frac{\partial^2 u}{\partial\theta^2}-R^3\frac{\partial^3 w}{\partial x^3}+\frac{R(1-\nu)}{2}\frac{\partial^3 w}{\partial x\partial\theta^2}\right)=-\frac{(1-\nu^2)}{Eh}q_x(x,\theta)e^{j\omega t} \tag{4.1}$$

$$\frac{R(1+\nu)}{2}\frac{\partial^2 u}{\partial x\partial\theta}+\frac{R^2(1-\nu)}{2}\frac{\partial^2 v}{\partial x^2}+\frac{\partial^2 v}{\partial\theta^2}-\frac{\rho R^2(1-\nu^2)}{E}\frac{\partial^2 v}{\partial t^2}+\frac{\partial w}{\partial\theta}+\xi\left(\frac{3R^2(1-\nu)}{2}\frac{\partial^2 v}{\partial x^2}-\frac{3R^2(3-\nu)}{2}\frac{\partial^3 w}{\partial x^2\partial\theta}\right)=-\frac{(1-\nu^2)}{Eh}q_\theta(x,\theta)e^{j\omega t} \tag{4.2}$$

and

$$R\nu\frac{\partial u}{\partial x}+\frac{\partial v}{\partial\theta}+w+\xi\nabla^4 w+\frac{\rho R^2(1-\nu^2)}{E}\frac{\partial^2 w}{\partial t^2}+\xi\left(\frac{R(1-\nu)}{2}\frac{\partial^3 u}{\partial x\partial\theta^2}-R^3\frac{\partial^3 u}{\partial x^3}-\frac{R^2(3-\nu)}{2}\frac{\partial^3 v}{\partial x^2\partial\theta}+w+2\frac{\partial^2 w}{\partial\theta^2}\right)=\frac{(1-\nu^2)}{Eh}q_r(x,\theta)e^{j\omega t}\ , \tag{4.3}$$

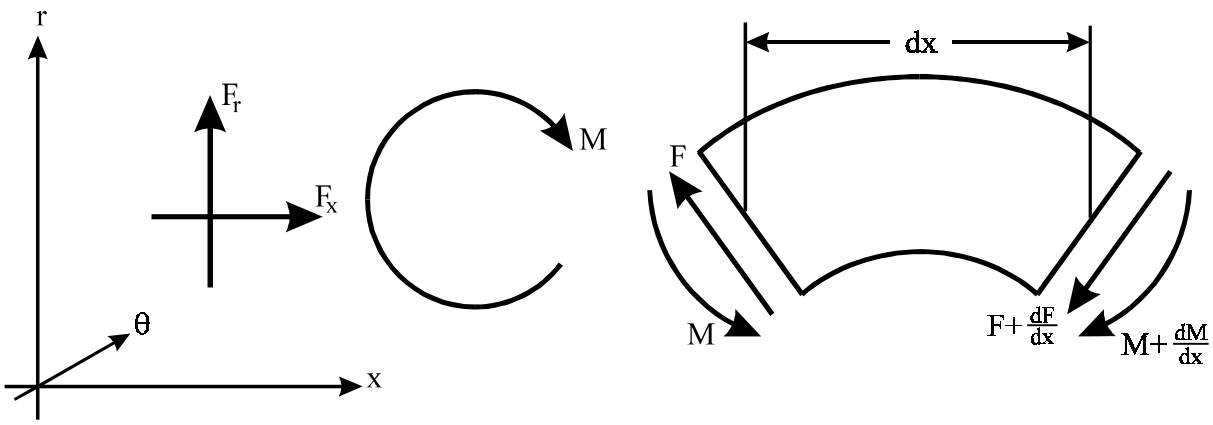

Figure 4.3 Sign conventions for forces and moments (conventions for forces and moments in the θ-plane are similar).

where R is the shell radius, h is the shell thickness, E is Young's modulus of elasticity, ν is Poisson's ratio, ρ is the shell density, $\xi = h^2/12R^2$, $\nabla^4 = \nabla^2\nabla^2$ is the square of the modified Laplacian operator $\nabla^2 = R^2\frac{\partial}{\partial x} + \frac{\partial}{\partial \theta}$, and $u(x,\theta,t)$, $v(x,\theta,t)$ and $w(x,\theta,t)$ are the displacements in the axial, tangential and radial directions respectively.

As the cylinder is closed, the following harmonic series solutions in θ can be assumed for the cylinder vibrational displacements in the x, y and z directions:

$$u(x, \theta, t) = \sum_{n=1}^{\infty} u_n(x) \cos(n\theta)\, e^{j\omega t} , \tag{4.4}$$

$$v(x, \theta, t) = \sum_{n=1}^{\infty} v_n(x) \sin(n\theta)\, e^{j\omega t} \tag{4.5}$$

and

$$w(x, \theta, t) = \sum_{n=1}^{\infty} w_n(x) \cos(n\theta)\, e^{j\omega t} , \tag{4.6}$$

where n is a mode number and ω is the angular frequency. Each of the eigenfunctions $u_n(x)$, $v_n(x)$ and $w_n(x)$ can be expressed in terms of modal wavenumbers k_{sn} as follows (Forsberg, 1964):

$$u_n(x) = \sum_{s=1}^{8} \beta_{sn} A_{sn} e^{k_{sn} x} , \tag{4.7}$$

$$v_n(x) = \sum_{s=1}^{8} \gamma_{sn} A_{sn} e^{k_{sn} x} \tag{4.8}$$

and

$$w_n(x) = \sum_{s=1}^{8} A_{sn} e^{k_{sn} x} , \tag{4.9}$$

where A_{sn}, β_{sn} and γ_{sn} are arbitrary constants.

4.2.2 Determining the wavenumbers *k* and constants β and γ

Substitution of Equations (4.4) - (4.9) into the homogeneous forms of Equations (4.1) - (4.3) yields

$$\sum_{n=0}^{\infty} \sum_{s=1}^{8} \left[\beta_{sn} \left(R^2 k_{sn}^2 - \frac{(1-\nu)}{2} n^2 + \rho \frac{(1-\nu^2)}{E} R^2 \omega^2 - \xi \frac{(1-\nu)}{2} n^2 \right) + \gamma_{sn} \left(\frac{(1+\nu)}{2} R n k_{sn} \right) + \left(\nu R k_{sn} - \xi R^3 k_{sn}^3 - \xi \frac{(1-\nu)}{2} R n^2 k_{sn} \right) \right] A_{sn} e^{k_{sn} x} \cos(n\theta) e^{j\omega t} = 0 , \tag{4.10}$$

$$\sum_{n=0}^{\infty}\sum_{s=1}^{8}\left[\beta_{sn}\left(-\frac{(1-\nu)}{2}Rnk_{sn}\right)+\gamma_{sn}\left(\frac{(1-\nu)}{2}R^2k_{sn}^2-n^2+\rho\frac{(1-\nu^2)}{E}R^2\omega^2+\xi\frac{3(1-\nu)}{2}R^2k_{sn}^2\right)+\left(-n+\xi\frac{(3-\nu)}{2}R^2nk_{sn}^2\right)\right]A_{sn}e^{k_{sn}x}\cos(n\theta)\,e^{j\omega t}=0 \tag{4.11}$$

and

$$\sum_{n=0}^{\infty}\sum_{s=1}^{8}\left[\beta_{sn}\left(\nu Rk_{sn}-\xi R^3k_{sn}^3-\xi\frac{(1-\nu)}{2}Rn^2k_{sn}\right)+\gamma_{sn}\left(n-\xi\frac{(3-\nu)}{2}R^2nk_{sn}^2\right)+\left(1+\xi R^4k_{sn}^4-2\xi R^2n^2k_{sn}^2+\xi n^4-\rho\frac{(1-\nu^2)}{E}R^2\omega^2+\xi-2\xi n^2\right)\right]A_{sn}e^{k_{sn}x}\cos(n\theta)\,e^{j\omega t}=0\ . \tag{4.12}$$

For a non-trivial solution valid over the surface of the cylinder, $A_{sn}e^{k_{sn}x}\cos(n\theta)\,e^{j\omega t}$ is not zero, and Equations (4.10) - (4.12) can be re-written equivalently in the matrix form

$$\boldsymbol{C}\boldsymbol{A}=\boldsymbol{0}\ , \tag{4.13}$$

where $\boldsymbol{A}=[\beta_{sn},\ \gamma_{sn},\ 1]^T$ (s = 1,8) and $\boldsymbol{C}$ contains the remainder of the coefficients. For homogeneous boundary conditions, the determinant of $\boldsymbol{C}$ must be non-zero for each n, leading to an eighth-order algebraic equation for k_{sn};

$$g_{s8}k_{sn}^8+g_{s6}k_{sn}^6+g_{s4}k_{sn}^4+g_{s2}k_{sn}^2+g_{s0}=0\ , \tag{4.14}$$

where

$$g_{s8}=\xi\left(KR^6-\xi KR^6\right)\ , \tag{4.15}$$

$$g_{s6}=\xi\left(HR^6+GKR^4-2KR^4n^2+\xi F^2R^2+C^2n^2R^4-2\xi FCR^3n-2\xi DR^4Kn^2-\xi\nu HR^6+2R^4K\right)\ , \tag{4.16}$$

$$g_{s4} = JKR^2 + \nu^2 KR^2 + \xi\left(-2n^2R^2(HR^2 + GK) + GHR^4 - 2FnR^2 + \xi F^2 G - 2C^2n^4R^2 - 2\xi FCDRn^3 + 2FC\nu Rn + 2CR^3n^2 - \xi D^2R^2n^4K + 2\nu HR^4 + 2DR^2n^2K - 2\xi HDR^4n^2\right), \tag{4.17}$$

$$g_{s2} = JHR^2 + JGK + n^2R^2 + JC^2n^2 - 2C\nu Rn^2 - \nu^2HR^2 + 2\nu DHR^2n^2 + \xi\left(-2n^2GHR^2 - 2FnG - \xi HD^2R^2n^4 + 2CDRn^4\right) \tag{4.18}$$

and

$$g_{s0} = JGH + Gn^2 , \tag{4.19}$$

where $B = \rho\frac{(1-\nu^2)}{E}R^2\omega^2$, $C = \frac{(1+\nu)}{2}R$, $D = \frac{(1-\nu)}{2}$, $F = \frac{(3-\nu)}{2}R^2n$, $G = B - Dn^2 - \xi Dn^2$, $H = -n^2 + B$, $J = 1 - B + \xi n^4 + \xi - 2\xi n^2$ and $K = DR^2 + \xi F/n$. As found by Forsberg (1964), all solutions of Equation (4.14) are of the form

$$k = \pm a,\ \pm jb,\ \pm(c \pm jd) \ . \tag{4.20}$$

where a, b, c and d are real quantities. This is different to the form of the solutions given by Flügge, because the inertia terms have been included here.

The constants β_{sn} and γ_{sn} can now be found from any two of Equations (4.10) - (4.12). Rearranging Equations (4.11) and (4.12) gives, for $n \geq 0$,

$$\beta_{sn} = \frac{(\xi R^4 k_{sn}^4 - 2\xi R^2 k_{sn}^2 n^2 + J)(Kk_{sn}^2 + H) + (n - \xi F k_{sn}^2)^2}{(\xi R^3 k_{sn}^3 + \xi DRk_{sn}n^2 - \nu Rk_{sn})(Kk_{sn}^2 + H) - (n - \xi Fk_{sn}^2)(Ck_{sn}n)} \tag{4.21}$$

and

$$\gamma_{sn} = \frac{(n - \xi F k_{sn}^2) + (C k_{sn} n)\beta_{sn}}{(K k_{sn}^2 + H)} \ . \tag{4.22}$$

The constants β_{sn} and γ_{sn} depend only on ω, ρ, ν, E, h and R. Note also that $\gamma_{s0} = 0$, as the $n = 0$ mode is a purely transverse expansion-contraction mode (see Figure 4.4).

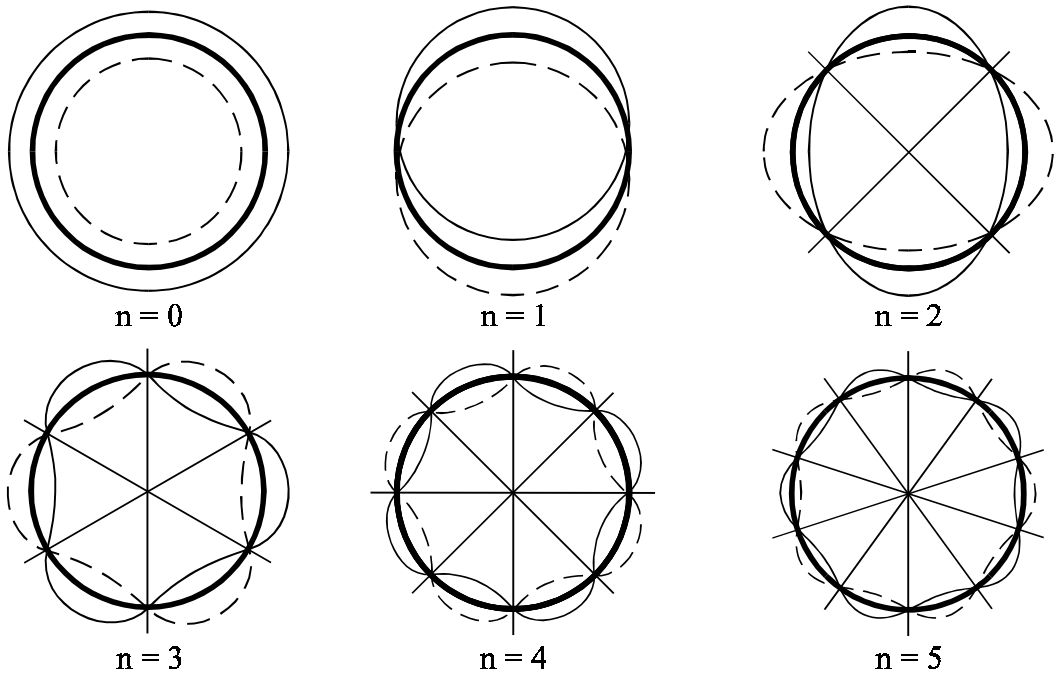

Figure 4.4 Circumferential modes of vibration.

On each side of an applied force or moment at $x = x_0$, each eigenfunction is a different linear combination of the terms $e^{k_{sn}x}$ ($i = 1,4$). For $x < x_0$,

$$u_{1n}(x) = \sum_{s=1}^{8} \beta_{sn} A_{1sn} e^{k_{sn}x} \ , \tag{4.23}$$

$$v_{1n}(x) = \sum_{s=1}^{8} \gamma_{sn} A_{1sn} e^{k_{sn}x} \ , \tag{4.24}$$

and

$$w_{1n}(x) = \sum_{s=1}^{8} A_{1sn} e^{k_{sn}x} \ . \tag{4.25}$$

For $x > x_0$,

$$u_{2n}(x) = \sum_{s=1}^{8} \beta_{sn} A_{2sn} e^{k_{sn}x} \ , \tag{4.26}$$

$$v_{2n}(x) = \sum_{s=1}^{8} \gamma_{sn} A_{2sn} e^{k_{sn}x} \ , \tag{4.27}$$

and

$$w_{2n}(x) = \sum_{s=1}^{8} A_{2sn} e^{k_{sn}x} \ . \tag{4.28}$$

To solve for the sixteen unknowns A_{1sn} and A_{2sn}, for s = 1,8, sixteen equations are required, comprising eight boundary conditions (four conditions at each end of the cylinder) and eight equilibrium conditions at the point of application x_0 of the force or moment, for each circumferential mode n of the cylinder vibration.

4.2.3 Boundary conditions at the cylinder ends

For the purposes of this work, two sets of boundary conditions will be examined; those

corresponding to a shell with simply supported ends, and those corresponding to a semi-infinite shell with the end at $x = 0$ modelled as simply supported.

4.2.3.1 Simply supported end conditions

The four boundary conditions corresponding to a simple support are $u = 0$, $v = 0$, $w = 0$ and $M_x = 0$ (Leissa 1973*a*), where M_x is the moment resultant in the x-plane and is given by

$$M_x = \frac{Eh^3}{12(1-\nu^2)}\left[-\frac{\partial^2 w}{\partial x^2} + \frac{\nu}{R^2}\frac{\partial v}{\partial \theta} - \frac{\nu}{R^2}\frac{\partial^2 w}{\partial \theta^2} + \frac{1}{R}\frac{\partial u}{\partial x}\right] . \tag{4.29}$$

In terms of the displacement unknowns, these boundary conditions for a simply supported end at $x = 0$ are

$$\sum_{s=1}^{8} \beta_{sn} A_{1sn} = 0 , \tag{4.30}$$

$$\sum_{s=1}^{8} \gamma_{sn} A_{1sn} = 0 , \tag{4.31}$$

$$\sum_{s=1}^{8} A_{1sn} = 0 \tag{4.32}$$

and

$$\sum_{s=1}^{8} \left[\frac{\nu n}{R^2}(\gamma_{sn} + n) + \frac{\beta_{sn}}{R}k_{sn} - k_{sn}^2\right] A_{1sn} = 0 . \tag{4.33}$$

The corresponding boundary conditions for a simply supported end at $x = L_x$ are

$$\sum_{s=1}^{8} \beta_{sn} A_{2sn} e^{k_{sn} L_x} = 0 \ , \tag{4.34}$$

$$\sum_{s=1}^{8} \gamma_{sn} A_{2sn} e^{k_{sn} L_x} = 0 \ , \tag{4.35}$$

$$\sum_{s=1}^{8} A_{2sn} e^{k_{sn} L_x} = 0 \tag{4.36}$$

and

$$\sum_{s=1}^{8} \left[\frac{\nu n}{R^2} (\gamma_{sn} + n) + \frac{\beta_{sn}}{R} k_{sn} - k_{sn}^2 \right] A_{2sn} e^{k_{sn} L_x} = 0 \ . \tag{4.37}$$

4.2.3.2 Infinite end conditions

An infinite end produces no reflections, so the boundary conditions corresponding to an infinite end at $x = L_x$ are

$$A_{21n} = 0 \ , \tag{4.38}$$

$$A_{23n} = 0 \ , \tag{4.39}$$

$$A_{25n} = 0 \tag{4.40}$$

and

$$A_{27n} = 0 \ . \tag{4.41}$$

4.2.4 Equilibrium conditions at the point of application of a force or moment

Requiring that the displacement and gradient in each direction be continuous at any point in the cylinder wall, the first six equilibrium conditions at $x = x_0$ which must be satisfied are

$$u_{1n} = u_{2n} \ , \tag{4.42}$$

$$\frac{\partial u_{1n}}{\partial x} = \frac{\partial u_{2n}}{\partial x} \ , \tag{4.43}$$

$$v_{1n} = v_{2n} \ , \tag{4.44}$$

$$\frac{\partial v_{1n}}{\partial x} = \frac{\partial v_{2n}}{\partial x} \ , \tag{4.45}$$

$$w_{1n} = w_{2n} \tag{4.46}$$

and

$$\frac{\partial w_{1n}}{\partial x} = \frac{\partial w_{2n}}{\partial x} \ . \tag{4.47}$$

The form of the excitation $q_r(x,\theta)$ will affect the higher order equilibrium conditions at $x = x_0$. In the following sections the response of the shell to a point force, a circumferential line force and a circumferential line moment is discussed.

4.2.4.1 Response of a shell to a radially acting point force

The response of the shell to a simple harmonic point force F_0 acting normal to the shell at position (x_0,θ_0) is considered. The excitation $q_r(x,\theta)$ in Equation (4.3) is replaced by $q_r(x,\theta) = RF_0\delta(x - x_0)\delta(\theta - \theta_0)$, where δ is the Dirac delta function. Replacing u, v and w by

Equations (4.4) - (4.6), dividing by $e^{j\omega t}$ and multiplying by cos($n\theta$), Equation (4.3) becomes

$$\begin{aligned}&\Bigg[R\nu u_n'(x) - \xi R^3 u_n'''(x) - \xi\frac{R(1-\nu)}{2}n^2 u_n'(x) + n v_n(x)\\ &\xi\frac{R^2(3-\nu)}{2}n v_n''(x) + w_n(x) + \xi R^4 w_n''''(x) - 2\xi R^2 n^2 w_n''(x) + \xi n^4 w_n(x)\\ &\quad - \frac{\rho R^2(1-\nu^2)}{E}\omega^2 w_n(x) + \xi w_n(x) - 2\xi n^2 w_n(x)\Bigg]\cos^2(n\theta)\\ &\qquad = \frac{R(1-\nu^2)}{Eh}F_0\delta(x-x_0)\delta(\theta-\theta_0)\cos(n\theta)\ .\end{aligned} \tag{4.48}$$

The integral with respect to θ around the circumference of the cylinder is taken, noting that

$$\int_0^{2\pi}\delta(\theta-\theta_0)\cos(n\theta)\,d\theta = \cos(n\theta_0)\ , \tag{4.49}$$

to find

$$\begin{aligned}&\pi\Bigg[R\nu u_n'(x) - \xi R^3 u_n'''(x) - \xi\frac{R(1-\nu)}{2}n^2 u_n'(x) + n v_n(x)\\ &\xi\frac{R^2(3-\nu)}{2}n v_n''(x) + w_n(x) + \xi R^4 w_n''''(x) - 2\xi R^2 n^2 w_n''(x) + \xi n^4 w_n(x)\\ &\quad - \frac{\rho R^2(1-\nu^2)}{E}\omega^2 w_n(x) + \xi w_n(x) - 2\xi n^2 w_n(x)\Bigg]\\ &\qquad = \frac{R(1-\nu^2)}{Eh}F_0\delta(x-x_0)\cos(n\theta_0)\ .\end{aligned} \tag{4.50}$$

Next, the integral with respect to x is taken between the limits x_0 - δ and x_0 + δ, using the conditions

$$\int_{x_0-\delta}^{x_0+\delta} w_n(x)\,dx \to 0 \ , \tag{4.51}$$

$$\int_{x_0-\delta}^{x_0+\delta} w_n'(x)\,dx \to 0 \tag{4.52}$$

and

$$\int_{x_0-\delta}^{x_0+\delta} w_n''(x)\,dx \to 0 \tag{4.53}$$

(similarly for $u_n(x)$ and $v_n(x)$) as $\delta \to 0$, to find

$$\pi\left[\xi R^4 w_n'''(x) - \xi R^3 u_n''(x)\right]_{x_0-\delta}^{x_0+\delta} = \frac{R(1-\nu^2)}{Eh} F_0 \cos(n\theta_0) \ , \tag{4.54}$$

or

$$\left[\frac{\partial^2 u_{1n}}{\partial x^2} - \frac{\partial^2 u_{2n}}{\partial x^2}\right] - R\left[\frac{\partial^3 w_{1n}}{\partial x^3} - \frac{\partial^3 w_{2n}}{\partial x^3}\right] = \frac{(1-\nu^2)}{\xi \pi R^2 Eh} F_0 \cos(n\theta_0) \ . \tag{4.55}$$

Finally, the integral with respect to x is taken again between the limits x_0 - δ and x_0 + δ to find the second order equilibrium condition

$$\frac{\partial^2 w_{1n}}{\partial x^2} = \frac{\partial^2 w_{2n}}{\partial x^2} \ . \tag{4.56}$$

4.2.4.2 Response of a shell to a circumferentially distributed line force

Instead of a point force, the excitation represented by $q_r(x,\theta)$ in Equation (4.3) is replaced by an array of N equally spaced point forces distributed along an arc parallel to the θ-axis between θ_1 and θ_2. These forces act at locations (x_0 , θ_k, $k = 1,N$) and each has a magnitude of F_0/N, so $q_r(x,\theta)$ in Equation (4.3) is replaced by $q_r(x,\theta) = \left(\frac{RF_0}{N}\right)\sum_{k=1}^{N}\delta(x - x_0)\delta(\theta - \theta_k)$. Following the method of Section (4.2.4.1), and using the relation

$$\lim_{N\to\infty}\left[\sum_{k=1}^{N}\frac{(\theta_2 - \theta_1)}{N}\cos(n\theta_k)\right] = \int_{\theta_1}^{\theta_2}\cos(n\theta)\,d\theta \ , \tag{4.57}$$

the second and third order equilibrium conditions at $x = x_0$ are

$$\frac{\partial^2 w_{1n}}{\partial x^2} = \frac{\partial^2 w_{2n}}{\partial x^2} \tag{4.58}$$

and

$$\left[\frac{\partial^2 u_{1n}}{\partial x^2} - \frac{\partial^2 u_{2n}}{\partial x^2}\right] - R\left[\frac{\partial^3 w_{1n}}{\partial x^3} - \frac{\partial^3 w_{2n}}{\partial x^3}\right] = \frac{(1 - \nu^2)}{\xi\pi n(\theta_2 - \theta_1)R^2Eh}F_0\left[\sin(n\theta_2) - \sin(n\theta_1)\right] . \tag{4.59}$$

4.2.4.3 Response of a shell to a circumferentially distributed line moment

The excitation represented by $q_r(x,\theta)$ in Equation (4.3) is replaced by a distributed line moment M_0 per unit length acting along an arc parallel to the θ-axis between θ_1 and θ_2. The excitation $q_r(x,\theta)$ is replaced by $q_r(x,\theta) = \frac{\partial M_x}{\partial x} = RM_0[\delta'(x - x_0)]\,[h(\theta - \theta_1) - h(\theta - \theta_2)]$, where h is the

unit step function. Following the method of Section (4.2.4.1), and using the relation

$$\int_0^{2\pi} h(\theta - \theta_1)\cos(n\theta)\,d\theta = \frac{\sin(n\theta_1)}{n}\ , \tag{4.60}$$

Equation (4.50) becomes

$$\begin{aligned}\pi\Big[&R\nu u_n'(x) - \xi R^3 u_n'''(x) - \xi\frac{R(1-\nu)}{2}n^2 u_n'(x) + n v_n(x)\\ &\xi\frac{R^2(3-\nu)}{2}n v_n''(x) + w_n(x) + \xi R^4 w_n''''(x) - 2\xi R^2 n^2 w_n''(x) + \xi n^4 w_n(\\ &-\frac{\rho R^2(1-\nu^2)}{E}\omega^2 w_n(x) + \xi w_n(x) - 2\xi n^2 w_n(x)\Big]\\ &= \frac{R(1-\nu^2)}{nEh}M_0\delta'(x-x_0)\Big[\sin(n\theta_2) - \sin(n\theta_1)\Big]\ .\end{aligned} \tag{4.61}$$

Next, the integral with respect to x is taken between the limits x_0 - δ and x_0 + δ to find

$$\pi\Big[\xi R^4 w_n'''(x) - \xi R^3 u_n''(x)\Big]_{x_0-\delta}^{x_0+\delta} = \frac{R(1-\nu^2)}{nEh}M_0\delta(x-x_0)\Big[\sin(n\theta_2) - \sin(n\theta_1)\Big] \tag{4.62}$$

or

$$\begin{aligned}&\left[\frac{\partial^2 u_{1n}}{\partial x^2} - \frac{\partial^2 u_{2n}}{\partial x^2}\right] - R\left[\frac{\partial^3 w_{1n}}{\partial x^3} - \frac{\partial^3 w_{2n}}{\partial x^3}\right]\\ &= \frac{(1-\nu^2)}{\xi\pi nR^2 Eh}M_0\delta(x-x_0)\Big[\sin(n\theta_2) - \sin(n\theta_1)\Big]\ .\end{aligned} \tag{4.63}$$

The integral with respect to x is taken again between the limits x_0 - δ and x_0 + δ to find the second order equilibrium condition

$$\frac{\partial^2 w_{1n}}{\partial x^2} - \frac{\partial^2 w_{2n}}{\partial x^2} = -\frac{(1-\nu^2)}{\xi \pi n R^3 E h} M_0 \left[\sin(n\theta_2) - \sin(n\theta_1)\right] . \tag{4.64}$$

Differentiation gives

$$\frac{\partial^3 w_{1n}}{\partial x^3} = \frac{\partial^3 w_{2n}}{\partial x^3} . \tag{4.65}$$

Taking four boundary conditions at each end of the shell from Equations (4.30) - (4.41), the six equilibrium condition Equations (4.42) - (4.47), and two further equilibrium conditions from Equations (4.55), (4.56), (4.58), (4.59), (4.64) and (4.65), sixteen equations in the sixteen unknowns A_{1sn} and A_{2sn} for s = 1,8 are obtained. These can be written in the form $\boldsymbol{\alpha X} = \boldsymbol{B}$. The solution vectors $\boldsymbol{X} = [A_{11n}\, A_{12n}\, A_{13n} \ldots A_{18n}\, A_{21n}\, A_{22n} \ldots A_{28n}]^T = \boldsymbol{\alpha}^{-1}\boldsymbol{B}$ can be used to characterise the response of a cylindrical shell to simple harmonic excitation by a single point force, a circumferentially distributed line force or a circumferentially distributed line moment.

4.2.5 Modelling the effects of the angle stiffener

The mass and stiffness of the angle stiffener may be significant. Given a cylindrical shell with some excitation q_r at axial position $x = x_0$ and an angle stiffener extending around the circumference of the cylinder at axial position $x = x_1$, as shown in Figure 4.5, three eigenfunction solutions of Equations (4.1) - (4.3) are now required.

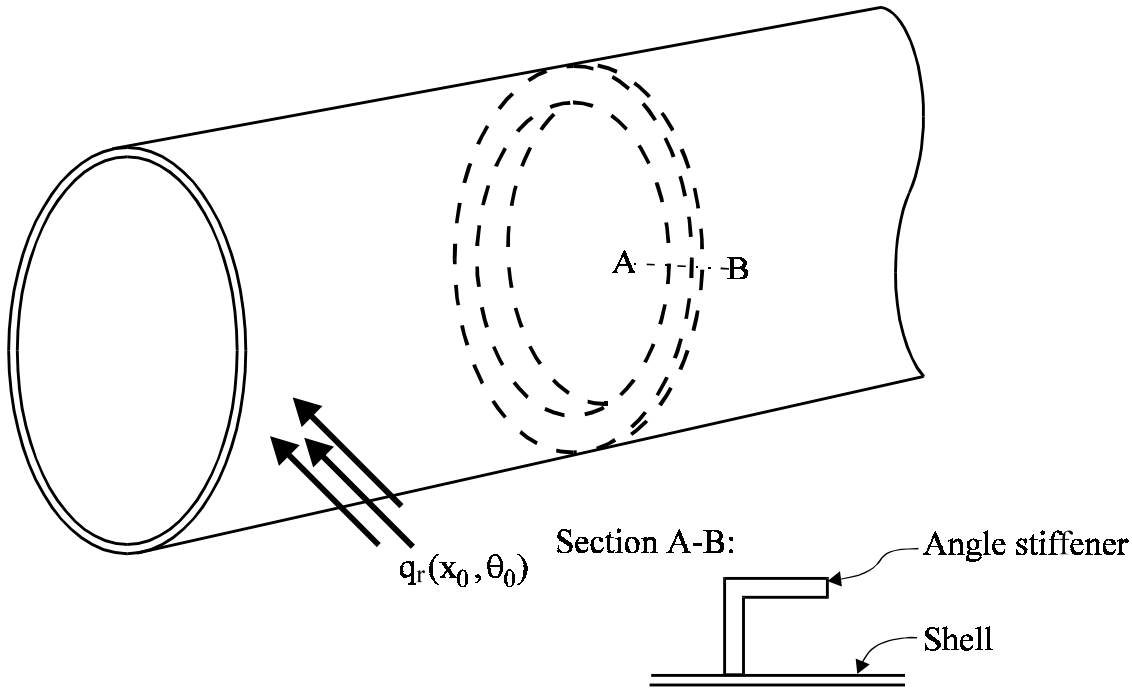

Figure 4.5 Semi-infinite cylinder with an excitation q_r and an angle stiffener.

For $x < x_0$

$$w_{1n}(x) = \sum_{s=1}^{8} A_{1sn} e^{k_{sn} x} \tag{4.66}$$

for $x_0 < x < x_1$,

$$w_{2n}(x) = \sum_{s=1}^{8} A_{2sn} e^{k_{sn} x} \tag{4.67}$$

and for $x > x_1$,

$$w_{3n}(x) = \sum_{s=1}^{8} A_{3sn} e^{k_{sn} x} \tag{4.68}$$

and similarly for u_{in} and v_{in} (i = 1,3). These eigenfunctions allow for reflection at the stiffener

location. Twenty four equations in the twenty four unknowns A_{isn}; i = 1,3; s = 1,8 are now required. In addition to the eight equilibrium conditions at $x = x_0$ which depend on the form of the excitation q_r, and the boundary conditions at each end of the shell, the equilibrium conditions which must be satisfied at the stiffener location $x = x_1$ are

$$u_{2n} = u_{3n} \ , \tag{4.69}$$

$$\frac{\partial u_{2n}}{\partial x} = \frac{\partial u_{3n}}{\partial x} \ , \tag{4.70}$$

$$v_{2n} = v_{3n} \ , \tag{4.71}$$

$$\frac{\partial v_{2n}}{\partial x} = \frac{\partial v_{3n}}{\partial x} \ , \tag{4.72}$$

$$w_{2n} = w_{3n} \ , \tag{4.73}$$

$$\frac{\partial w_{2n}}{\partial x} = \frac{\partial w_{3n}}{\partial x} \ , \tag{4.74}$$

$$\frac{\partial^2 w_{2n}}{\partial x^2} = \frac{\partial^2 w_{3n}}{\partial x^2} \ , \tag{4.75}$$

and

$$\left[\frac{\partial^2 u_{1n}}{\partial x^2} - \frac{\partial^2 u_{2n}}{\partial x^2}\right] - R\left[\frac{\partial^3 w_{1n}}{\partial x^3} - \frac{\partial^3 w_{2n}}{\partial x^3}\right] = -\frac{(1-\nu^2)}{2\xi\pi R^2 Eh}\left(K_a + m_a\omega^2\right) w_n(x_0) \ . \tag{4.76}$$

where K_a is the stiffness and m_a the mass per unit length of the stiffener. If the angle stiffener is very rigid compared to the cylinder, Equations (4.73) and (4.76) can be replaced by the following two conditions:

$$w_{2n} = 0 \tag{4.77}$$

and

$$w_{3n} = 0 \ . \tag{4.78}$$

4.2.6 Minimising vibration using piezoceramic actuators and an angle stiffener

For any force or moment excitation, the twenty four equations in twenty four unknowns can be written in the form $\boldsymbol{\alpha X = B}$, where $\boldsymbol{X} = [A_{11n}\, A_{12n}\, A_{13n} \ldots A_{18n}\, A_{21n}\, A_{22n} \ldots A_{28n}\, A_{31n}\, A_{32n} \ldots A_{38n}]^T$, and $\boldsymbol{B}$ is a column vector. When the excitation position is to the left of the stiffener location, i.e. $x_0 < x_1$, $\boldsymbol{B}$ has a non zero excitation term in the fifteenth row for excitation by a line moment about an arc parallel to the θ-axis or the sixteenth row otherwise. For a simply supported cylindrical shell with the end at $x = 0$ free, $\boldsymbol{\alpha}$ is given by Equation (4.79), except in the case of a distributed moment excitation when row sixteen is replaced by Equation (4.65). If the excitation position is to the right of the stiffener location, i.e. $x_0 > x_1$, then a similar analysis is followed, resulting in an excitation vector $\boldsymbol{B}$ with the non zero term in the twenty third row for excitation by a line moment about an arc parallel to the θ-axis or the twenty fourth row otherwise, and $\boldsymbol{\alpha}$ is given by Equation (4.80), except in the case of a distributed moment excitation when row twenty four is replaced by Equation (4.65). For the cylinder with the right hand end modelled as infinite, the equations corresponding to rows 5-8 of the matrix $\boldsymbol{\alpha}$ are replaced by Equations (4.38) - (4.41). For both sets of boundary conditions, the matrix equation

$\boldsymbol{\alpha X = B}$ can be solved for $\boldsymbol{X}$ for any type of excitation and the result can be used with Equations (4.4) - (4.9) and (4.66) - (4.68) to calculate the corresponding cylinder response.

Figure 4.6 shows the semi-infinite shell with primary forces F_{p1} and F_{p2} located at $x = x_p$, $\theta = \theta_{p1}$ and $\theta = \theta_{p2}$, control actuators at $x = x_c$ and a line of error sensors at $x = x_e$. Figure 4.7 shows the resultant forces and moments applied to the cylinder by the control actuators. Control forces F_{ci}, i =1,6 act at (x_{c2}, θ_{ci}, i = 1,6), with the distributed force F_c and distributed moment M_c acting about the circumference parallel to the θ-axis at (x_{c1}, $\theta = 0$ to $\theta = 2\pi$).

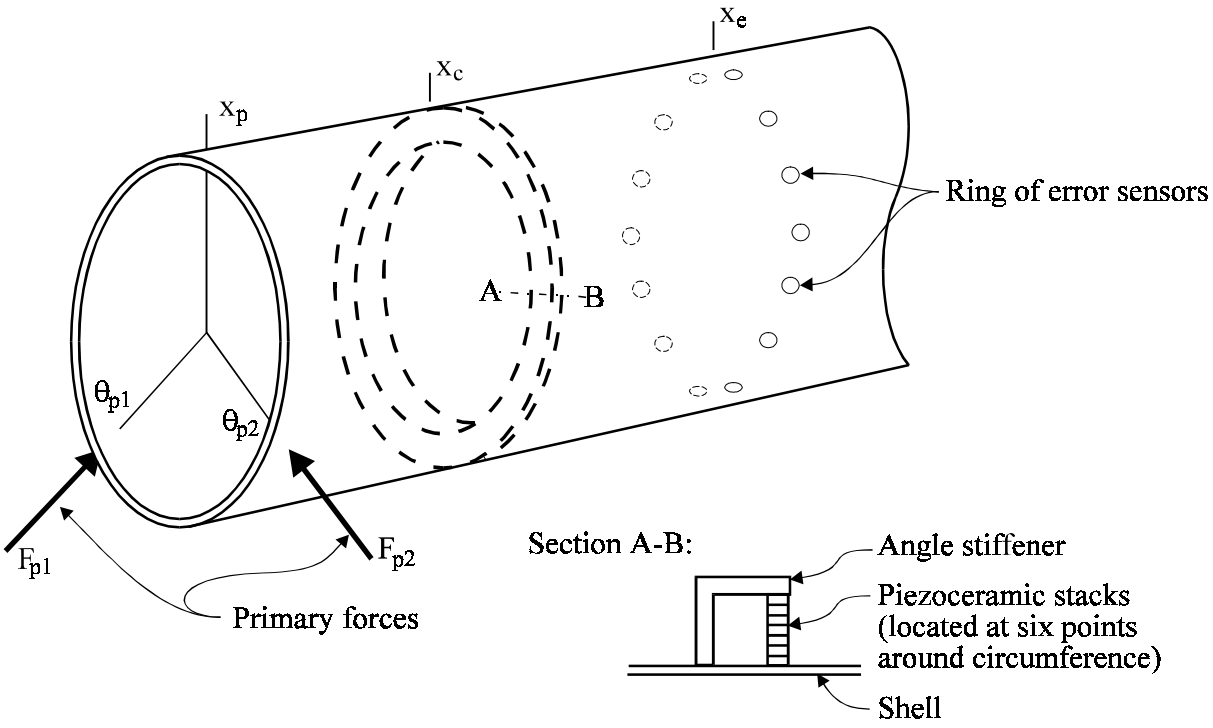

Figure 4.6 Semi-infinite cylinder showing primary forces, control actuators, angle stiffener and ring of error sensors.

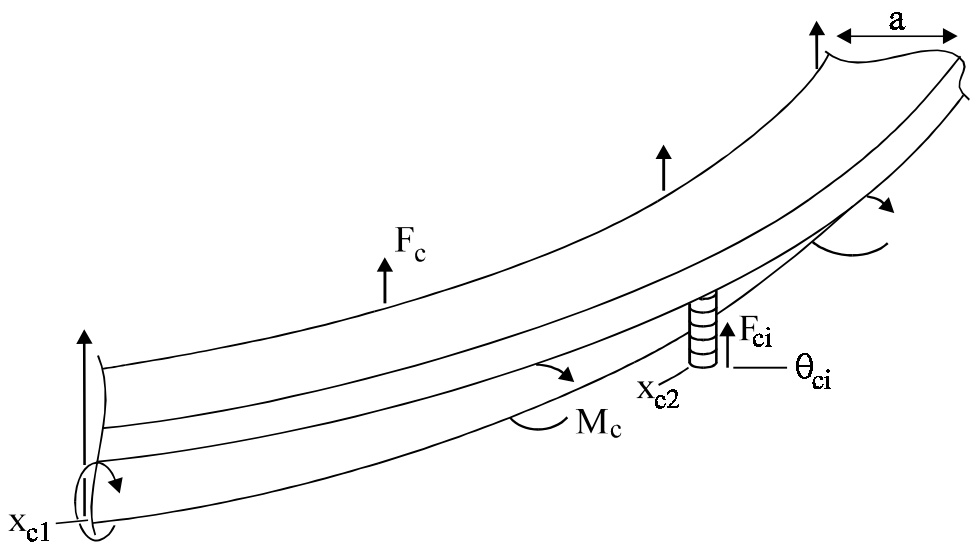

Figure 4.7 Part-stiffener and control actuator showing control forces and moment.

$$\boldsymbol{\alpha} = \begin{bmatrix}
\beta_{1n} & \cdots & \beta_{8n} & 0 & \cdots \\
\gamma_{1n} & \cdots & \gamma_{8n} & 0 & \cdots \\
1 & \cdots & 1 & 0 & \cdots \\
\frac{\nu n}{R^2}(\gamma_{1n}+n)+\frac{\beta_{1n}}{R}k_{1n}-k_{1n}^2 & \cdots & \frac{\nu n}{R^2}(\gamma_{8n}+n)+\frac{\beta_{8n}}{R}k_{8n}-k_{8n}^2 & 0 & \cdots \\
0 & \cdots & 0 & 0 & \cdots \\
0 & \cdots & 0 & 0 & \cdots \\
0 & \cdots & 0 & 0 & \cdots \\
0 & \cdots & 0 & 0 & \cdots \\
\beta_{1n}e^{k_{1n}x_0} & \cdots & \beta_{8n}e^{k_{8n}x_0} & -\beta_{1n}e^{k_{1n}x_0} & \cdots \\
\beta_{1n}k_{1n}e^{k_{1n}x_0} & \cdots & \beta_{8n}k_{8n}e^{k_{8n}x_0} & -\beta_{1n}k_{1n}e^{k_{1n}x_0} & \cdots \\
\gamma_{1n}e^{k_{1n}x_0} & \cdots & \gamma_{8n}e^{k_{8n}x_0} & -\gamma_{1n}e^{k_{1n}x_0} & \cdots \\
\gamma_{1n}k_{1n}e^{k_{1n}x_0} & \cdots & \gamma_{8n}k_{8n}e^{k_{8n}x_0} & -\gamma_{1n}k_{1n}e^{k_{1n}x_0} & \cdots \\
e^{k_{1n}x_0} & \cdots & e^{k_{8n}x_0} & -e^{k_{1n}x_0} & \cdots \\
k_{1n}e^{k_{1n}x_0} & \cdots & k_{8n}e^{k_{8n}x_0} & -k_{1n}e^{k_{1n}x_0} & \cdots \\
k_{1n}^2e^{k_{1n}x_0} & \cdots & k_{8n}^2e^{k_{8n}x_0} & -k_{1n}^2e^{k_{1n}x_0} & \cdots \\
(\beta_{1n}-Rk_{1n})k_{1n}^2e^{k_{1n}x_0} & \cdots & (\beta_{8n}-Rk_{8n})k_{8n}^2e^{k_{8n}x_0} & -(\beta_{1n}-Rk_{1n})k_{1n}^2e^{k_{1n}x_0} & \cdots \\
0 & \cdots & 0 & \beta_{1n}e^{k_{1n}x_1} & \cdots \\
0 & \cdots & 0 & \beta_{1n}k_{1n}e^{k_{1n}x_1} & \cdots \\
0 & \cdots & 0 & \gamma_{1n}e^{k_{1n}x_1} & \cdots \\
0 & \cdots & 0 & \gamma_{1n}k_{1n}e^{k_{1n}x_1} & \cdots \\
0 & \cdots & 0 & e^{k_{1n}x_1} & \cdots \\
0 & \cdots & 0 & 0 & \cdots \\
0 & \cdots & 0 & k_{1n}e^{k_{1n}x_1} & \cdots \\
0 & \cdots & 0 & k_{1n}^2e^{k_{1n}x_1} & \cdots
\end{bmatrix}$$

$$
\begin{bmatrix}
\cdots & 0 & 0 & \cdots & 0 \\
\cdots & 0 & 0 & \cdots & 0 \\
\cdots & 0 & 0 & \cdots & 0 \\
\cdots & 0 & 0 & \cdots & 0 \\
\cdots & 0 & \beta_{1n} e^{k_{1n} L_x} & \cdots & \beta_{8n} e^{k_{8n} L_x} \\
\cdots & 0 & \gamma_{1n} e^{k_{1n} L_x} & \cdots & \gamma_{8n} e^{k_{8n} L_x} \\
\cdots & 0 & e^{k_{1n} L_x} & \cdots & e^{k_{8n} L_x} \\
\cdots & 0 & \left(\frac{\nu n}{R^2} (\gamma_{1n} + n) + \frac{\beta_{1n}}{R} k_{1n} - k_{1n}^2 \right) e^{k_{1n} L_x} & \cdots & \left(\frac{\nu n}{R^2} (\gamma_{8n} + n) + \frac{\beta_{8n}}{R} k_{8n} - k_{8n}^2 \right)_{8n} e^{k_{8n} L_x} \\
\cdots & -\beta_{8n} e^{k_{8n} x_0} & 0 & \cdots & 0 \\
\cdots & -\beta_{8n} k_{8n} e^{k_{8n} x_0} & 0 & \cdots & 0 \\
\cdots & -\gamma_{8n} e^{k_{8n} x_0} & 0 & \cdots & 0 \\
\cdots & -\gamma_{8n} k_{8n} e^{k_{8n} x_0} & 0 & \cdots & 0 \\
\cdots & -e^{k_{8n} x_0} & 0 & \cdots & 0 \\
\cdots & -k_{8n} e^{k_{8n} x_0} & 0 & \cdots & 0 \\
\cdots & -k_{8n}^2 e^{k_{8n} x_0} & 0 & \cdots & 0 \\
\cdots & -(\beta_{8n} - R k_{8n}) k_{8n}^2 e^{k_{8n} x_0} & 0 & \cdots & 0 \\
\cdots & \beta_{8n} e^{k_{8n} x_1} & -\beta_{1n} e^{k_{1n} x_1} & \cdots & -\beta_{8n} e^{k_{8n} x_1} \\
\cdots & \beta_{8n} k_{8n} e^{k_{8n} x_1} & -\beta_{1n} k_{1n} e^{k_{1n} x_1} & \cdots & -\beta_{8n} k_{8n} e^{k_{8n} x_1} \\
\cdots & \gamma_{8n} e^{k_{8n} x_1} & -\gamma_{1n} e^{k_{1n} x_1} & \cdots & -\gamma_{8n} e^{k_{8n} x_1} \\
\cdots & \gamma_{8n} k_{8n} e^{k_{8n} x_1} & -\gamma_{1n} k_{1n} e^{k_{1n} x_1} & \cdots & -\gamma_{8n} k_{8n} e^{k_{8n} x_1} \\
\cdots & e^{k_{8n} x_1} & 0 & \cdots & 0 \\
\cdots & 0 & -e^{k_{1n} x_1} & \cdots & -e^{k_{8n} x_1} \\
\cdots & k_{8n} e^{k_{8n} x_1} & -k_{1n} e^{k_{1n} x_1} & \cdots & -k_{8n} e^{k_{8n} x_1} \\
\cdots & k_{8n}^2 e^{k_{8n} x_1} & -k_{1n}^2 e^{k_{1n} x_1} & \cdots & -k_{8n}^2 e^{k_{8n} x_1}
\end{bmatrix}
\tag{4.79}
$$

$$\boldsymbol{\alpha} = \begin{bmatrix}
\beta_{1n} & \cdots & \beta_{8n} & 0 & \cdots \\
\gamma_{1n} & \cdots & \gamma_{8n} & 0 & \cdots \\
1 & \cdots & 1 & 0 & \cdots \\
\frac{\nu n}{R^2}(\gamma_{1n}+n)+\frac{\beta_{1n}}{R}k_{1n}-k_{1n}^2 & \cdots & \frac{\nu n}{R^2}(\gamma_{8n}+n)+\frac{\beta_{8n}}{R}k_{8n}-k_{8n}^2 & 0 & \cdots \\
0 & \cdots & 0 & 0 & \cdots \\
0 & \cdots & 0 & 0 & \cdots \\
0 & \cdots & 0 & 0 & \cdots \\
0 & \cdots & 0 & 0 & \cdots \\
\beta_{1n}e^{k_{1n}x_1} & \cdots & \beta_{8n}e^{k_{8n}x_1} & -\beta_{1n}e^{k_{1n}x_1} & \cdots \\
\beta_{1n}k_{1n}e^{k_{1n}x_1} & \cdots & \beta_{8n}k_{8n}e^{k_{8n}x_1} & -\beta_{1n}k_{1n}e^{k_{1n}x_1} & \cdots \\
\gamma_{1n}e^{k_{1n}x_1} & \cdots & \gamma_{8n}e^{k_{8n}x_1} & -\gamma_{1n}e^{k_{1n}x_1} & \cdots \\
\gamma_{1n}k_{1n}e^{k_{1n}x_1} & \cdots & \gamma_{8n}k_{8n}e^{k_{8n}x_1} & -\gamma_{1n}k_{1n}e^{k_{1n}x_1} & \cdots \\
e^{k_{1n}x_1} & \cdots & e^{k_{8n}x_1} & 0 & \cdots \\
0 & \cdots & 0 & -e^{k_{1n}x_1} & \cdots \\
k_{1n}e^{k_{1n}x_1} & \cdots & k_{8n}e^{k_{8n}x_1} & -k_{1n}e^{k_{1n}x_1} & \cdots \\
k_{1n}^2e^{k_{1n}x_1} & \cdots & k_{8n}^2e^{k_{8n}x_1} & -k_{1n}^2e^{k_{1n}x_1} & \cdots \\
0 & \cdots & 0 & \beta_{1n}e^{k_{1n}x_0} & \cdots \\
0 & \cdots & 0 & \beta_{1n}k_{1n}e^{k_{1n}x_0} & \cdots \\
0 & \cdots & 0 & \gamma_{1n}e^{k_{1n}x_0} & \cdots \\
0 & \cdots & 0 & \gamma_{1n}k_{1n}e^{k_{1n}x_0} & \cdots \\
0 & \cdots & 0 & e^{k_{1n}x_0} & \cdots \\
0 & \cdots & 0 & k_{1n}e^{k_{1n}x_0} & \cdots \\
0 & \cdots & 0 & k_{1n}^2e^{k_{1n}x_0} & \cdots \\
0 & \cdots & 0 & (\beta_{1n}-Rk_{1n})k_{2n}^2e^{k_{1n}x_0} & \cdots
\end{bmatrix}$$

$$
\begin{bmatrix}
\cdots & 0 & 0 & \cdots & 0 \\
\cdots & 0 & 0 & \cdots & 0 \\
\cdots & 0 & 0 & \cdots & 0 \\
\cdots & 0 & 0 & \cdots & 0 \\
\cdots & 0 & \beta_{1n} e^{k_{1n} L_x} & \cdots & \beta_{8n} e^{k_{8n} L_x} \\
\cdots & 0 & \gamma_{1n} e^{k_{1n} L_x} & \cdots & \gamma_{8n} e^{k_{8n} L_x} \\
\cdots & 0 & e^{k_{1n} L_x} & \cdots & e^{k_{8n} L_x} \\
\cdots & 0 & \left(\frac{\nu n}{R^2} (\gamma_{1n} + n) + \frac{\beta_{1n}}{R} k_{1n} - k_{1n}^2 \right) e^{k_{1n} L_x} & \cdots & \left(\frac{\nu n}{R^2} (\gamma_{8n} + n) + \frac{\beta_{8n}}{R} k_{8n} - k_{8n}^2 \right) e^{k_{8n} L_x} \\
\cdots & -\beta_{8n} e^{k_{8n} x_1} & 0 & \cdots & 0 \\
\cdots & -\beta_{8n} k_{8n} e^{k_{8n} x_1} & 0 & \cdots & 0 \\
\cdots & -\gamma_{8n} e^{k_{8n} x_1} & 0 & \cdots & 0 \\
\cdots & -\gamma_{8n} k_{8n} e^{k_{8n} x_1} & 0 & \cdots & 0 \\
\cdots & 0 & 0 & \cdots & 0 \\
\cdots & e^{k_{8n} x_1} & 0 & \cdots & 0 \\
\cdots & -k_{8n} e^{k_{8n} x_1} & 0 & \cdots & 0 \\
\cdots & -k_{8n}^2 e^{k_{8n} x_1} & 0 & \cdots & 0 \\
\cdots & \beta_{8n} e^{k_{8n} x_0} & -\beta_{1n} e^{k_{1n} x_0} & \cdots & -\beta_{8n} e^{k_{8n} x_0} \\
\cdots & \beta_{8n} k_{8n} e^{k_{8n} x_0} & -\beta_{1n} k_{1n} e^{k_{1n} x_0} & \cdots & -\beta_{8n} k_{8n} e^{k_{8n} x_0} \\
\cdots & \gamma_{8n} e^{k_{8n} x_0} & -\gamma_{1n} e^{k_{1n} x_0} & \cdots & -\gamma_{8n} e^{k_{8n} x_0} \\
\cdots & \gamma_{8n} k_{8n} e^{k_{8n} x_0} & -\gamma_{1n} k_{1n} e^{k_{1n} x_0} & \cdots & -\gamma_{8n} k_{8n} e^{k_{8n} x_0} \\
\cdots & e^{k_{8n} x_0} & -e^{k_{1n} x_0} & \cdots & -e^{k_{8n} x_0} \\
\cdots & k_{8n} e^{k_{8n} x_0} & -k_{1n} e^{k_{1n} x_0} & \cdots & -k_{8n} e^{k_{8n} x_0} \\
\cdots & k_{8n}^2 e^{k_{8n} x_0} & -k_{1n}^2 e^{k_{1n} x_0} & \cdots & -k_{8n}^2 e^{k_{8n} x_0} \\
\cdots & -(\beta_{1n} - R k_{1n}) k_{1n}^2 e^{k_{1n} x_0} & (\beta_{1n} - R k_{1n}) k_{1n}^2 e^{k_{1n} x_0} & \cdots & -(\beta_{8n} - R k_{8n}) k_{8n}^2 e^{k_{8n} x_0}
\end{bmatrix}
$$

(4.80)

The cylinder response at any location (x,θ) to a particular excitation located at x_0, with a ring stiffener located at x_1 is (omitting the time dependent terms $e^{j\omega t}$)

$$u(x,\theta) = \sum_{n=1}^{\infty} [\boldsymbol{X}_\beta^T \boldsymbol{E}(x)]\cos(n\theta) \ , \tag{4.81}$$

$$v(x,\theta) = \sum_{n=1}^{\infty} ([\boldsymbol{X}_\gamma]^T \boldsymbol{E}(x))\cos(n\theta) \ , \tag{4.82}$$

and

$$w(x,\theta)6 = \sum_{n=1}^{\infty} (\boldsymbol{X}^T \boldsymbol{E}(x))\cos(n\theta) \ , \tag{4.83}$$

where $X_\beta = \beta_i X_i$ and $X_\gamma = \gamma_i X_i$ for $i = 1,8$, and for $x < x_0$ and $x < x_1$,

$$\boldsymbol{E} = \left[e^{k_{1n}x} \ \ e^{k_{2n}x} \ \ . \ . \ . \ e^{k_{7n}x} \ \ e^{k_{8n}x} \ \ 0 \ \ 0 \ \ . \ . \ . \ \ 0 \ \ 0\right]^T . \tag{4.84}$$

for $x_0 < x < x_1$ or $x_1 < x < x_0$,

$$\boldsymbol{E} = \left[0 \ \ 0 \ . \ . \ . \ 0 \ \ 0 \ \ e^{k_{1n}x} \ \ e^{k_{2n}x} \ \ . \ . \ . \ e^{k_{7n}x} \ \ e^{k_{8n}x} \ \ 0 \ \ 0 \ . \ . \ . \ 0 \ \ 0\right]^T . \tag{4.85}$$

and for $x > x_0$ and $x > x_1$,

$$\boldsymbol{E} = \left[0 \ \ 0 \ \ . \ . \ . \ 0 \ \ 0 \ \ e^{k_{1n}x} \ \ e^{k_{2n}x} \ \ . \ . \ . \ e^{k_{7n}x} \ \ e^{k_{8n}x}\right]^T . \tag{4.86}$$

By summation of the displacements corresponding to each force and moment, the total radial displacement is found to be

$$\begin{aligned} w &= \sum_{i=1}^{2} \left(w_{F_{pi}}\right) + \sum_{i=1}^{6} \left(w_{F_{ci}}\right) + w_{F_c} + w_{M_c} \\ &= \sum_{n=1}^{\infty} \left(\sum_{i=1}^{2} \left[\boldsymbol{X}_{\boldsymbol{F_{pi}}}^{\boldsymbol{T}} \boldsymbol{E}(x)\right] + \sum_{i=1}^{6} \left[\boldsymbol{X}_{\boldsymbol{F_{ci}}}^{\boldsymbol{T}} \boldsymbol{E}(x)\right] + \boldsymbol{X}_{\boldsymbol{F_c}}^{\boldsymbol{T}} \boldsymbol{E}(x) + \boldsymbol{X}_{\boldsymbol{M_c}}^{\boldsymbol{T}} \boldsymbol{E}(x) \right) \cos(n\theta) \ . \end{aligned} \tag{4.87}$$

where the subscripts F_{pi}, F_{ci}, F_c and M_c on w and $\boldsymbol{X}$ refer to the corresponding excitation force or moment.

As the excitation vector $\boldsymbol{B}$ has a non-zero element in one row only, the solution vector $\boldsymbol{X}$ can be written in terms of a single column of the inverse $\boldsymbol{\alpha}^{-1}$:

$$\boldsymbol{X} = (\boldsymbol{\alpha}^{-1})_{k,15} B_{15} \quad , \quad (\boldsymbol{\alpha}^{-1})_{k,16} B_{16} \quad , \quad (\boldsymbol{\alpha}^{-1})_{k,23} B_{23} \quad , \; or \quad (\boldsymbol{\alpha}^{-1})_{k,24} B_{24} \; , \; k = 1,24 \; , \tag{4.88}$$

where $(\boldsymbol{\alpha}^{-1})_{k,i}$ is the k^{th} element in the i^{th} column of the inverse of $\boldsymbol{\alpha}$ and B_i is the i^{th} element (the non-zero element) of $\boldsymbol{B}$. The value taken by i depends on the form and location of the excitation, as discussed previously.

4.2.6.1 Control sources driven by the same signal

If the three control actuators are driven by the same signal, then $F_{ci} = -F_s$, say, for $i = 1,6$. The i^{th} actuator also generates a distributed force of total magnitude F_s and a distributed moment of total magnitude $x_a F_s$, acting along an arc between $(\theta_{i-1} + \theta_i)/2$ and $(\theta_i + \theta_{i+1})/2$ where x_a is the width of the stiffener flange. Additionally, if the primary shakers are driven by the same signal, then $F_{p1i} = F_{p2i}$ $(i = 1,2) = F_p$, say. Defining

$$\boldsymbol{F_{Pi}} = \frac{(1-\nu^2)}{\pi \xi R^2 E h} \left\langle \boldsymbol{\alpha}^{-1}_{\boldsymbol{F}_{pi}} \right\rangle^T_{k,16} \qquad (i = 1,2) \; , \tag{4.89}$$

$$\boldsymbol{F_{Ci}} = -\frac{(1-\nu^2)}{\pi \xi R^2 E h} \left\langle \boldsymbol{\alpha}^{-1}_{\boldsymbol{F}_{ci}} \right\rangle^T_{k,24} \qquad (i = 1,6) \; , \tag{4.90}$$

$$\left\langle \boldsymbol{F_C} \right\rangle_i = \frac{2(1-\nu^2)}{\pi \xi R^2 E h \left[\theta_{(i+1)} - \theta_{(i-1)}\right]} \left\langle \boldsymbol{\alpha}_{\boldsymbol{F_c}}^{-1} \right\rangle_{k,16}^T \qquad (i = 1,6) \tag{4.91}$$

and

$$\left\langle \boldsymbol{M_C} \right\rangle_i = \frac{(1-\nu^2)}{\pi \xi R^3 E h} \left\langle \boldsymbol{\alpha}_{\boldsymbol{M_c}}^{-1} \right\rangle_{k,15}^T \qquad (i = 1,6) \ . \tag{4.92}$$

Substituting Equations (4.89)-(4.92) into Equation (4.87) and rearranging gives

$$w(x,\theta) = \sum_{n=1}^{\infty} \left\{ \left[\sum_{i=1}^{2} \boldsymbol{F_{Pi}} \cos(n\theta_{pi}) \right] F_p + \left[\sum_{i=1}^{6} \left(\boldsymbol{F_{Ci}} \cos(n\theta_{ci}) + \frac{\left\langle \boldsymbol{F_C} \right\rangle_i + x_a \left\langle \boldsymbol{M_C} \right\rangle_i}{n} \left[\sin\left(\frac{n\theta_{(i+1)} + n\theta_i}{2} \right) - \sin\left(\frac{n\theta_{(i-1)} + n\theta_i}{2} \right) \right] F_s \right\} \boldsymbol{E}(x) \cos(n\theta) \right. \right. \ , \tag{4.93}$$

or

$$w(x,\theta) = w_p(x,\theta) F_p + w_s(x,\theta) F_s \ , \tag{4.94}$$

where

$$w_p(x,\theta) = \sum_{n=1}^{\infty} \left\{ \left[\sum_{i=1}^{2} \boldsymbol{F_{Pi}} \cos(n\theta_{pi}) \right] \right\} \boldsymbol{E}(x) \cos(n\theta) \tag{4.95}$$

and

$$w_s(x,\theta) = 6 \sum_{n=1}^{\infty} \left\{ \left[\sum_{i=1}^{6} \left(\boldsymbol{F_{Ci}} \cos(n\theta_{ci}) + \frac{\left\langle \boldsymbol{F_C} \right\rangle_i + x_a \left\langle \boldsymbol{M_C} \right\rangle_i}{n} \left[\sin\left(\frac{n\theta_{(i+1)} + n\theta_i}{2} \right) - \sin\left(\frac{n\theta_{(i-1)} + n\theta_i}{2} \right) \right] F_s \right\} \boldsymbol{E}(x) \cos(n\theta) \right. \right. \ . \tag{4.96}$$

The radial acceleration around the ring at $x = x_e$ is to be minimised. The mean square of the displacement defined in Equation (4.94) is integrated around the circumference of the cylinder:

$$\int_0^{2\pi} |w(x_e,\theta)|^2 d\theta = \int_0^{2\pi} |F_p w_p(x_e,\theta) + F_s w_s(x_e,\theta)|^2 d\theta \ . \tag{4.97}$$

Noting that $|z|^2 = z\bar{z}$ (where $\bar{z}$ is the complex conjugate of z), and writing $F_s = F_{sr} + jF_{sj}$,

$$\begin{aligned}\int_0^{2\pi} |w(x_e,\theta)|^2 d\theta = \int_0^{2\pi} \Big(& |F_p|^2 |w_p|^2 + F_p w_p \overline{w_s}(F_{sr} - jF_{sj}) + \\ & \overline{F_p w_p} w_s (F_{sr} + jF_{sj}) + (F_{sr}^2 + F_{sj}^2)|w_s|^2 \Big) d\theta \ .\end{aligned} \tag{4.98}$$

The partial derivatives of Equation (4.98) with respect to the real and imaginary components of the control force are taken and set equal to zero to find

$$\frac{\partial(\ \ )}{\partial F_{sr}} = \int_0^{2\pi} \left(F_p w_p \overline{w_s} + \overline{F_p w_p} w_s + 2F_{sr}|w_s|^2 \right) d\theta = 0 \tag{4.99}$$

and

$$j\frac{\partial(\ \ )}{\partial F_{sj}} = \int_0^{2\pi} \left(F_p w_p \overline{w_s} - \overline{F_p w_p} w_s + 2jF_{sj}|w_s|^2 \right) d\theta = 0 \ . \tag{4.100}$$

Adding Equations (4.99) and (4.100) gives

$$\int_0^{2\pi} \left(F_p w_p \overline{w_s} + F_s |w_s|^2 \right) d\theta = 0 \ . \tag{4.101}$$

The optimal control force F_s required to minimise normal acceleration at the ring of error sensors can thus be calculated by

$$F_s = -F_p \frac{\int_0^{2\pi} w_p(x_e,\theta)\,\overline{w_s(x_e,\theta)}\,d\theta}{\int_0^{2\pi} |w_s(x_e,\theta)|^2 d\theta} \,. \tag{4.102}$$

4.2.6.2 Control sources driven independently

If the six control actuators are driven independently, then a similar analysis is followed; however, six equations instead of one result from integrating the mean square of the displacement defined in Equation (4.94) and setting the partial derivatives of the integration with respect to the real and imaginary components of each control force equal to zero. The optimal control forces F_{si}, i = 1,6 required to minimise acceleration at the ring of error sensors can be calculated by

$$\begin{bmatrix} F_{s1} \\ F_{s2} \\ \cdot \\ \cdot \\ \cdot \\ F_{s6} \end{bmatrix} = -F_p \begin{bmatrix} \int_0^{2\pi} w_1\overline{w_1}d\theta & \int_0^{2\pi} w_2\overline{w_1}d\theta & \cdots & \int_0^{2\pi} w_6\overline{w_1}d\theta \\ \int_0^{2\pi} w_1\overline{w_2}d\theta & \int_0^{2\pi} w_2\overline{w_2}d\theta & \cdots & \int_0^{2\pi} w_6\overline{w_2}d\theta \\ \vdots & \vdots & \ddots & \vdots \\ \int_0^{2\pi} w_1\overline{w_6}d\theta & \int_0^{2\pi} w_2\overline{w_6}d\theta & \cdots & \int_0^{2\pi} w_6\overline{w_6}d\theta \end{bmatrix}^{-1} \begin{bmatrix} \int_0^{2\pi} w_p\overline{w_1}d\theta \\ \int_0^{2\pi} w_p\overline{w_2}d\theta \\ \vdots \\ \int_0^{2\pi} w_p\overline{w_6}d\theta \end{bmatrix} \tag{4.103}$$

4.2.6.3 Discrete error sensors

If the sum of the squares of the vibration amplitude measured at Q discrete points (x_e,θ_{qe}), q = 1,Q is used as the error signal instead of the integral around the circumference of the cylinder at location x_e, Equation (4.103) becomes

$$\begin{bmatrix} F_{s1} \\ F_{s2} \\ \cdot \\ \cdot \\ \cdot \\ F_{s6} \end{bmatrix} = -F_p \begin{bmatrix} \sum_{q=1}^{Q} w_1\overline{w_1} & \sum_{q=1}^{Q} w_2\overline{w_1} & \cdots & \sum_{q=1}^{Q} w_6\overline{w_1} \\ \sum_{q=1}^{Q} w_1\overline{w_2} & \sum_{q=1}^{Q} w_2\overline{w_2} & \cdots & \sum_{q=1}^{Q} w_6\overline{w_2} \\ \vdots & \vdots & \ddots & \vdots \\ \sum_{q=1}^{Q} w_1\overline{w_6} & \sum_{q=1}^{Q} w_2\overline{w_6} & \cdots & \sum_{q=1}^{Q} w_6\overline{w_6} \end{bmatrix}^{-1} \begin{bmatrix} \sum_{q=1}^{Q} w_p\overline{w_1} \\ \sum_{q=1}^{Q} w_p\overline{w_2} \\ \vdots \\ \sum_{q=1}^{Q} w_p\overline{w_6} \end{bmatrix} \tag{4.104}$$

where

$$w_i = w_i(x_e, \theta_{qe}) \ . \tag{4.105}$$

4.2.7 Natural frequencies

Leissa (1973*a*) gives the characteristic equation for the free vibration frequencies of a cylinder derived from the Flügge equations of motion:

$$\begin{aligned} \Omega^6 - \left[1 + \frac{1}{2}(3 - \nu)(n^2 + \lambda^2) + \xi(n^2 + \lambda^2)^2\right]\Omega^4 + \frac{1}{2}(1 - \nu)\Big[(3 + 2\nu)\lambda^2 + n^2 + \\ (n^2 + \lambda^2)^2 + \frac{(3 - \nu)}{(1 - \nu)}\xi(n^2 + \lambda^2)^2\Big]\Omega^2 - \frac{1}{2}(1 - \nu)\Big[(1 - \nu^2)\lambda^4 + \xi\{(n^2 + \lambda^2)^4 + \\ 2(2 - \nu)\lambda^2 n^2 + n^4 - 2\xi\nu\lambda^6 - 6\lambda^4 n^2 - 2(4 - \nu)\lambda^2 n^4 - 2n^6\}\Big] \end{aligned} \tag{4.106}$$

where $\lambda = m\pi R/L_x$, n is the circumferential mode number, m is the axial mode number, and the frequency parameter Ω is given by

$$\Omega = \omega\left(\frac{\rho(1 - \nu^2)R^2}{E}\right)^{\frac{1}{2}} \tag{4.107}$$

The natural frequencies ω can be obtained from Equation (4.107) by substitution of the real, positive solutions Ω from Equation (4.106).

4.3 NUMERICAL RESULTS

The theoretical model developed in the previous section was programmed in Fortran. The coefficient matrices $\boldsymbol{\alpha}$ (see Equations (4.79) and (4.80)) were close to singular. To obtain an accurate solution, 16-bit data types were required. The program consisted of about 3000 lines and, for a typical set of results, took 2 days C.P.U. time to run on a SPARC-20 computer.

The discussion that follows examines the effect of varying forcing frequency, control source location and error sensor location on the active control of vibration in cylinders with two sets of boundary conditions. In both models the end at $x = 0$ was modelled as simply supported. In one model, the end at $x = L_x$ was also modelled as simply supported and in the second model the cylinder was modelled as semi-infinite in the x-direction. The cylinder parameters (including location of the control source, primary source and error sensor) are listed in Table 4.1, and the excitation frequency was 132 Hz. These values are adhered to unless otherwise stated. The stiffener was assumed to be very stiff in comparison to the cylinder.

4.3.1 Acceleration distributions for controlled and uncontrolled cases

Figures 4.8 and 4.9 show the uncontrolled radial acceleration amplitude distribution in dB for the semi-infinite and finite cylinders. The cylinder has been "unrolled" in the figures so that the acceleration distribution can be seen more easily. The shape of the curves is very similar for the two cases, apart from near the end $x = 2.0$m where the acceleration of the finite cylinder is zero. It can be seen from the nature of the response that the near field effects become insignificant within a few centimetres of the points of discontinuity.

Table 4.1

Cylinder Parameters for Numerical and Experimental Results

Parameter	Value
Cylinder length L_x	2.0 m
Cylinder radius R	0.25 m
Cylinder thickness h	0.003 m
Young's modulus E	210 GPa
Primary source location x_p	0.025 m
Primary source locations θ_{p1}, θ_{p2}	$\pi/6$ rad, $3\pi/4$ rad
Control source location x_1	0.5 m
Control source locations θ_{c1}, θ_{c2}, θ_{c3}, θ_{c4}, θ_{c5}, θ_{c6}	$\pi/6$, $3\pi/4$, $29\pi/24$, $19\pi/12$, $15\pi/8$, 0 rad
Stiffener flange length a	0.05 m
Error sensor location x_e	1.0 m
Excitation frequency f	132 Hz

Unlike the corresponding plate and beam cases, there is no clear evidence of the existence of standing wave fields either upstream or downstream of the stiffener location on the finite or infinite cylinders. This is because the nodes that occur in the standing wave on a cylinder occur at large separations.

Let x_s be the separation between axial nodes in a standing wave. For a beam, $x_s = \lambda_b/2$ where λ_b is the flexural wavelength of vibration in a beam given by Equation (2.50), because vibration in a beam is one-dimensional. The path length corresponding to a mode is simply the length of the beam. In the case of a plate, the total path length corresponding to a mode may consist of a combination of plate widths and lengths, and similarly for a cylinder the path length may consist of a combination of cylinder circumferences and lengths. Generally, for plates and cylinders, $x_s \neq \lambda_b/2$, where the flexural wavelength of vibration in a plate is given by Equation (3.59) and in a cylinder is given by Pan and Hansen (1995*b*):

$$\lambda_b = \frac{1}{f}\left(\frac{Eh^2\omega^2}{12\rho(1-\nu^2)R^4} \right)^{\frac{1}{4}} . \tag{4.108}$$

In the far field of vibration, the eigenfunction describing the dependence of the displacement of a cylinder, plate or beam on axial coordinate x is given by, for each across-plate mode or circumferential cylinder mode n,

$$w_n(x) = A_3 e^{jb_n x} + A_4 e^{-jb_n x} . \tag{4.109}$$

Equation (4.109) is similar to Equations (2.2), (3.3) and (4.25), but retaining only the terms with no real (decaying) exponential part. The total displacement $w_n(x)$ is the sum of the displacement contributed by each mode n. Axial nodes in the displacement amplitude occur when $w_n(x)$ is at a minimum. Dropping the coefficients A_3 and A_4, differentiating Equation (4.109) and setting the result equal to zero gives

$$jb_n e^{jb_{nx}} - jb_n e^{jb_n x} = 0 \ . \tag{4.110}$$

Minima in Equation (4.109) occur when

$$\sin(b_n x) = 0 \ . \tag{4.111}$$

Nodes in the standing wave in the axial direction are thus separated by intervals

$$x_{sn} = \frac{\pi}{b_n} \ , \tag{4.112}$$

where *n* represents the number of the cross-plate mode on plate structures and circumferential mode on cylindrical structures. The mode number *n* has no significance on beams.

Considering the fixed beam described in Section 2.2, the finite plate described in Section 3.2 and the finite cylinder described in Section 4.2, the following table can be established comparing the distance between axial nodes. It can be seen from Table 4.2 that a cylinder of similar radius and thickness to those considered in this chapter would need to be about 25m long before a standing wave node could be observed. The distance between axial nodes on cylinders is typically much larger than for beams or plates.

Table 4.2

Comparison of Axial Node Separation in Beams, Plates and Cylinders

Mode n	Beam ($\lambda_b/2 = 0.2412$m) x_{sn} (m)	Plate ($\lambda_b/2 = 0.1793$m) x_{sn} (m)	Cylinder ($\lambda_b/2 = 0.9501$m) x_{sn} (m)
1	0.2412	0.1921	23.09
2	0.2412	0.2573	26.85
3	0.2412	0.4521	27.93
4	0.2412	0.1744	28.29
5	0.2412	0.1205	28.29
6	0.2412	0.0941	28.29
7	0.2412	0.0779	28.29
8	0.2412	0.0667	28.29

Close examination of Figure 4.9 reveals a slight decrease in acceleration amplitude between the stiffener location and the right hand end. This is due to the standing wave effect; the acceleration level begins to curve towards a minimum that would occur a half-wavelength away were the cylinder long enough. There is no decrease in acceleration level to the right of the stiffener location in Figure 4.8 as no standing wave exists downstream of the stiffener on the semi-infinite cylinder.

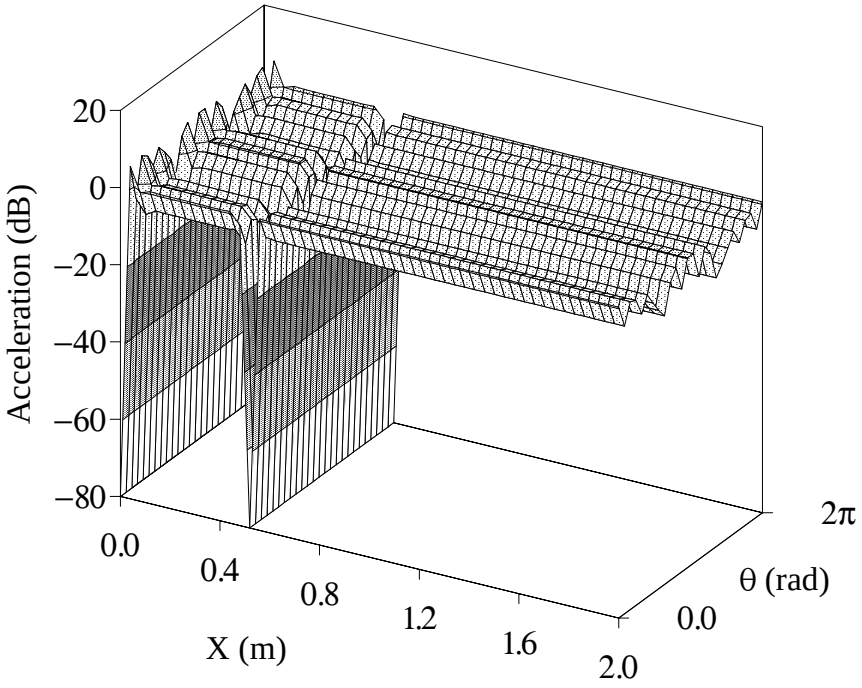

Figure 4.8 Uncontrolled semi-infinite cylinder radial acceleration distribution. The end at x = 0 is modelled as simply supported.

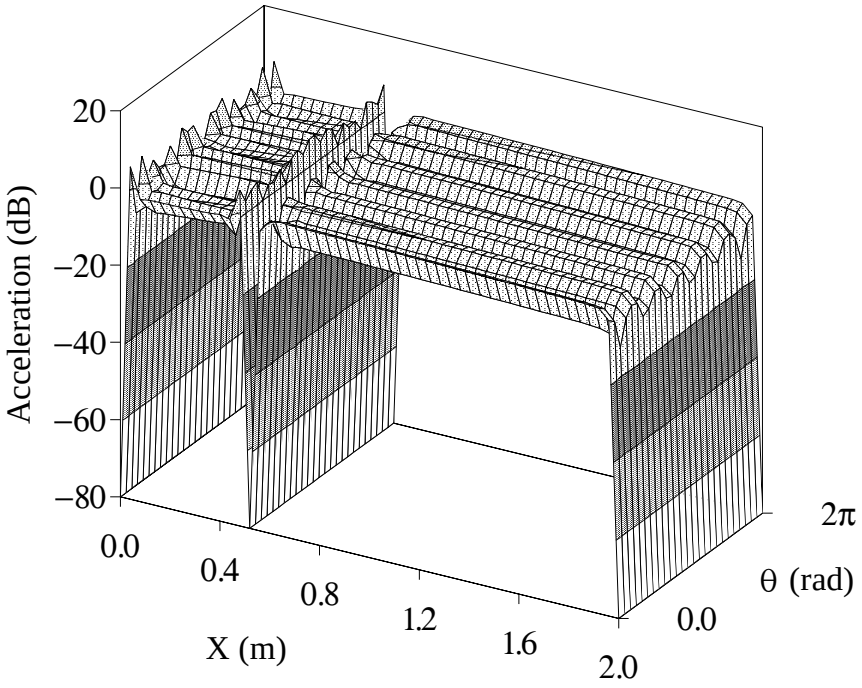

Figure 4.9 Uncontrolled finite cylinder radial acceleration distribution. The ends at x = 0 and x = 2.0 are modelled as simply supported.

Figures 4.10 and 4.11 show the controlled acceleration amplitude distributions for the semi-infinite and finite cylinders with the six control sources driven by the same signal. The acceleration level is only marginally reduced. The calculated reduction in acceleration amplitude downstream of the ring of error sensors is only about 3 dB. Several higher-order circumferential modes contribute significantly to the vibration response of the cylinder so control sources driven by a common signal are not capable of significantly reducing the overall vibration level.

Figures 4.12 and 4.13 show the controlled acceleration amplitude distributions for the semi-infinite and finite cylinders with the six control sources driven independently. The acceleration level is at a minimum at the error sensor location (x_e = 1.0m). The calculated reduction in acceleration amplitude downstream of the error sensor is a little over 40 dB for the semi infinite cylinder and a little under 40 dB for the finite cylinder.

Figures 4.14 - 4.21 show the axial and tangential acceleration distributions corresponding to the radial acceleration distributions given in Figures 4.8, 4.9, 4.12 and 4.13. Only radial vibration at the ring of error sensors is optimally reduced in the controlled cases. The figures show that controlling radial vibration also results in significant reduction of vibration in the axial and tangential directions (between 30 and 40 dB attenuation). Axial acceleration levels are of a similar order as radial acceleration levels, while tangential acceleration is generally a few dB less. In theory, tangential acceleration modes are out of phase with radial and axial acceleration modes, and this can also been seen on the figures.

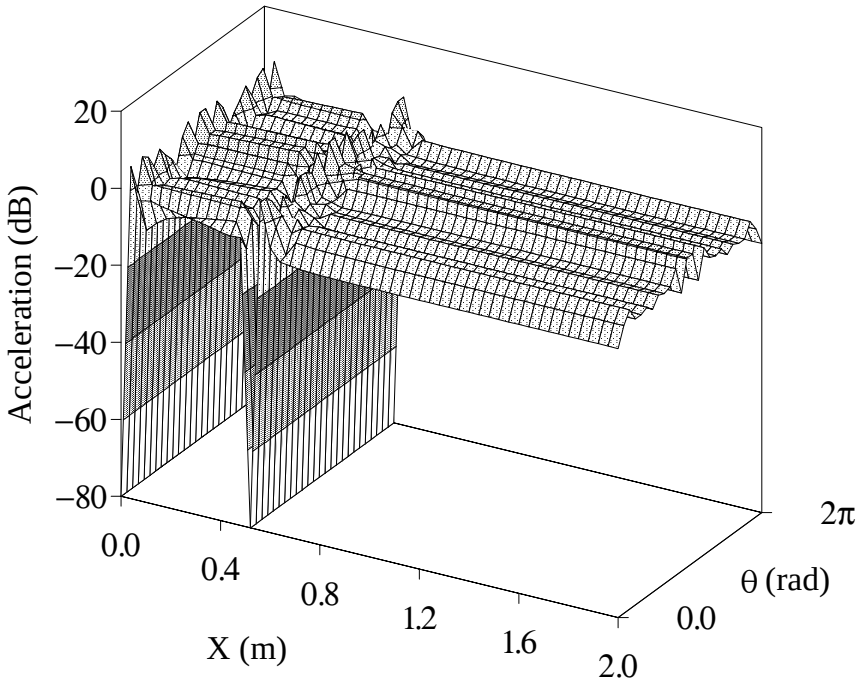

Figure 4.10 Controlled semi-infinite cylinder radial acceleration distribution - control sources driven by the same signal.

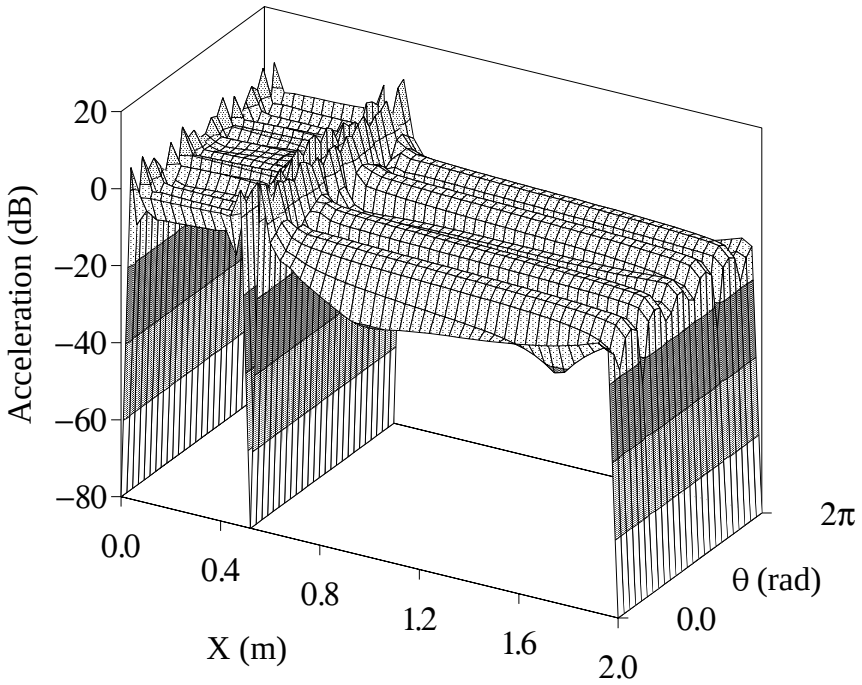

Figure 4.11 Controlled finite cylinder radial acceleration distribution - control sources driven by the same signal.

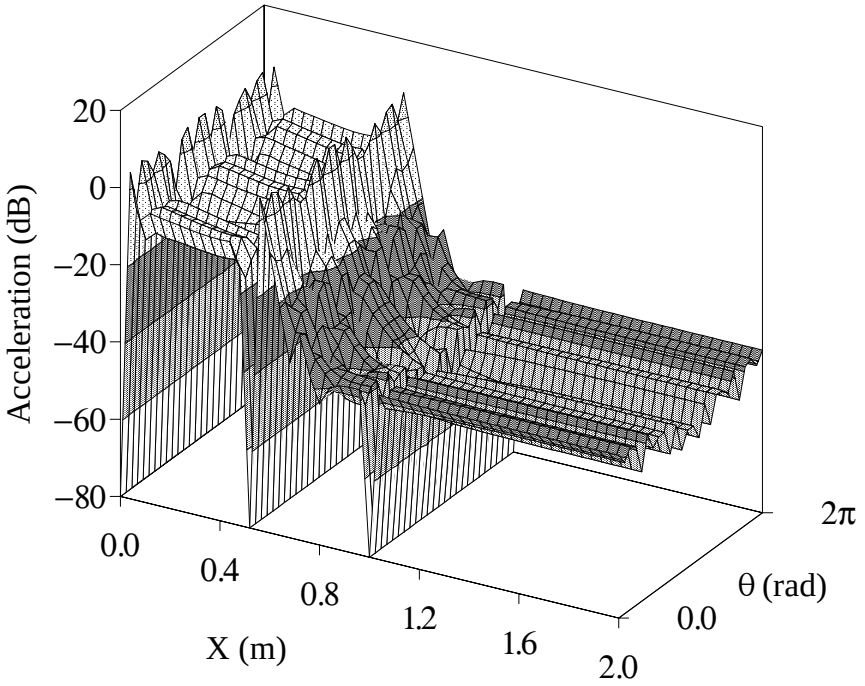

Figure 4.12 Controlled semi-infinite cylinder radial acceleration distribution - control sources driven independently.

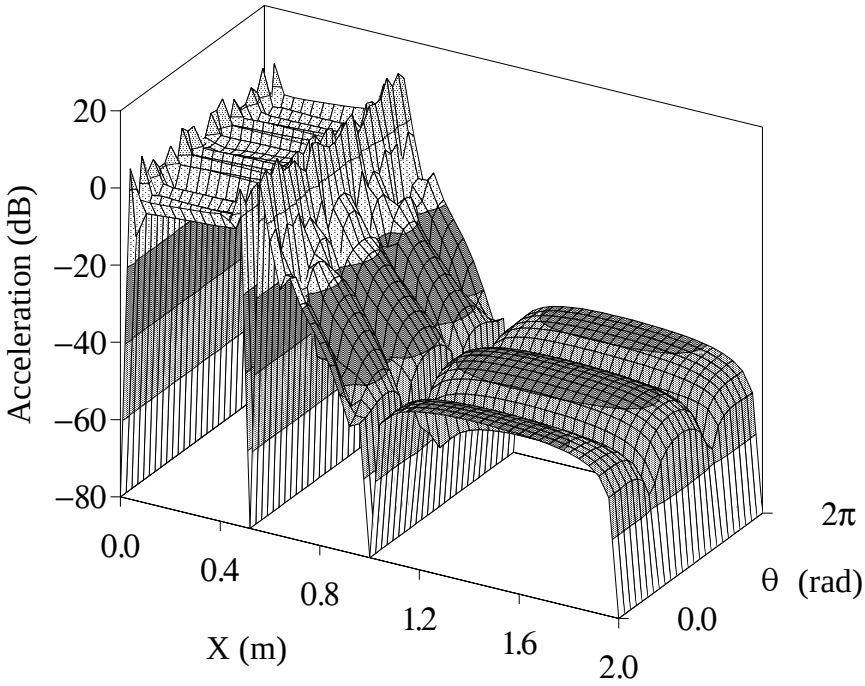

Figure 4.13 Controlled finite cylinder radial acceleration distribution - control sources driven independently.

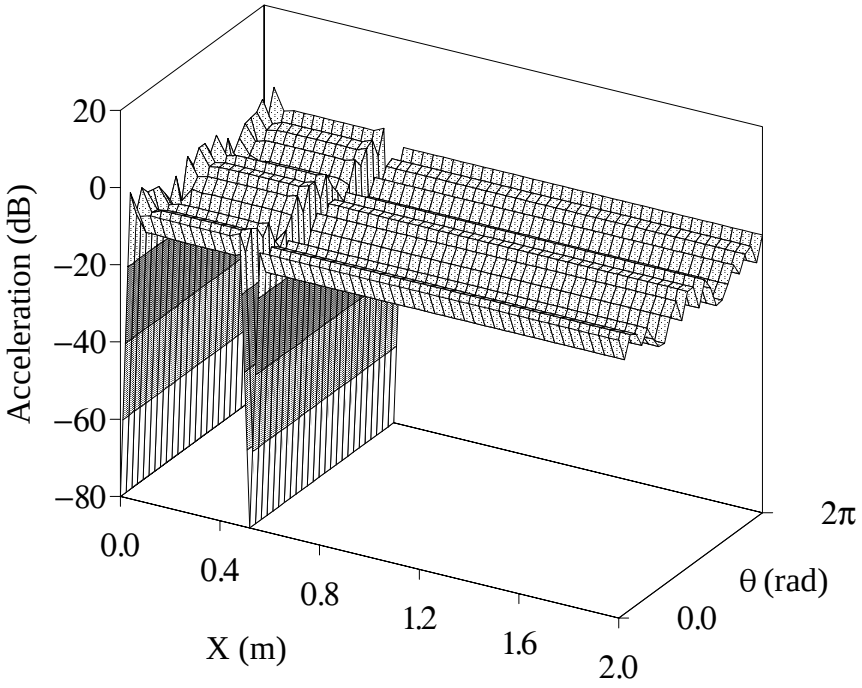

Figure 4.14 Uncontrolled semi-finite cylinder axial acceleration distribution.

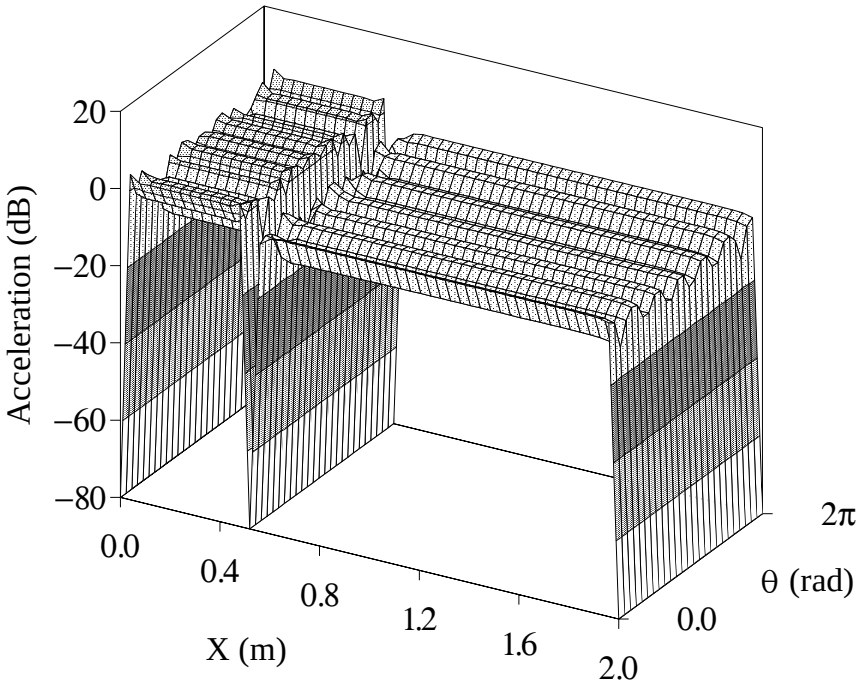

Figure 4.15 Uncontrolled finite cylinder axial acceleration distribution.

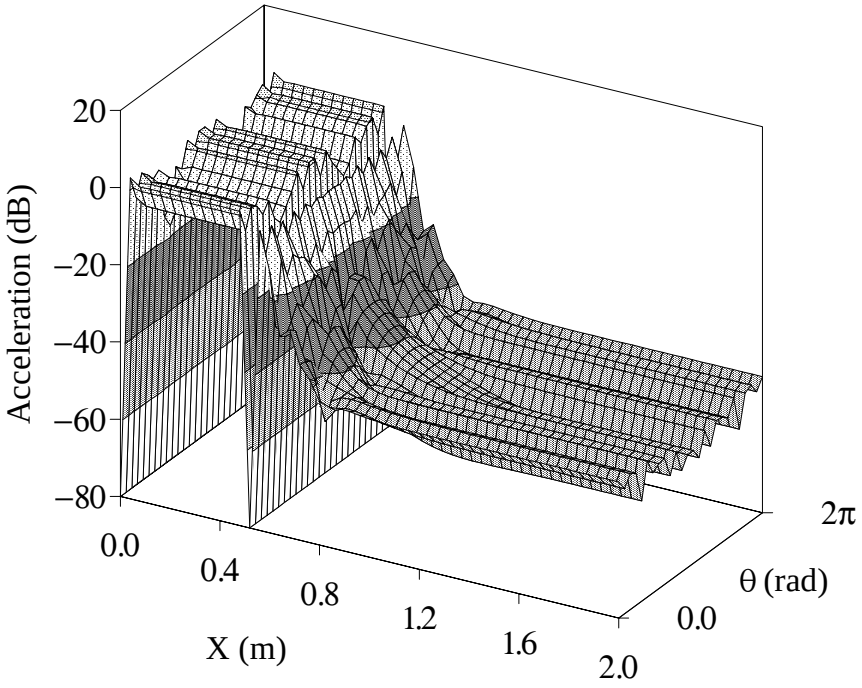

Figure 4.16 Controlled semi-finite cylinder axial acceleration distribution - control sources driven independently.

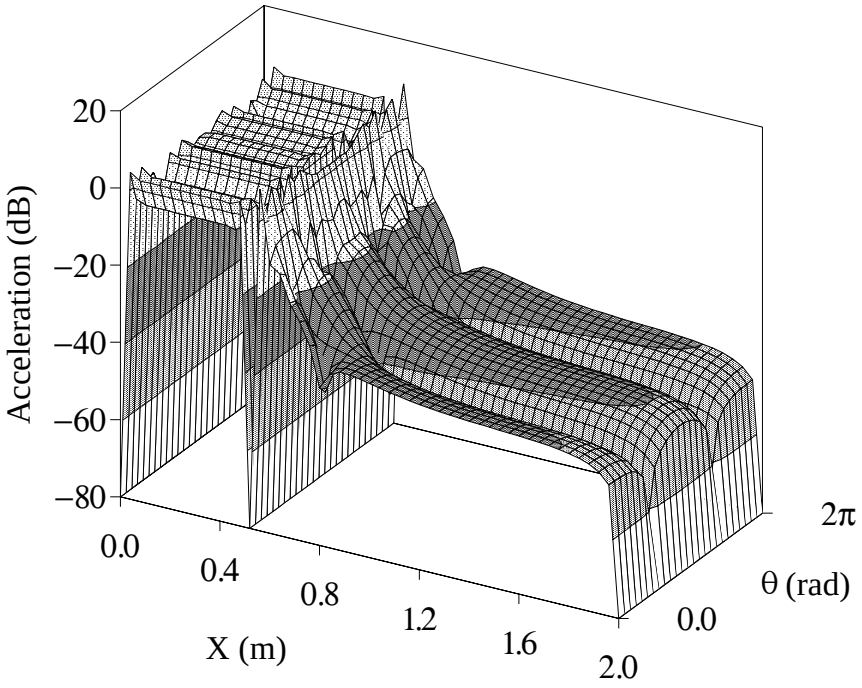

Figure 4.17 Controlled finite cylinder axial acceleration distribution - control sources driven independently.

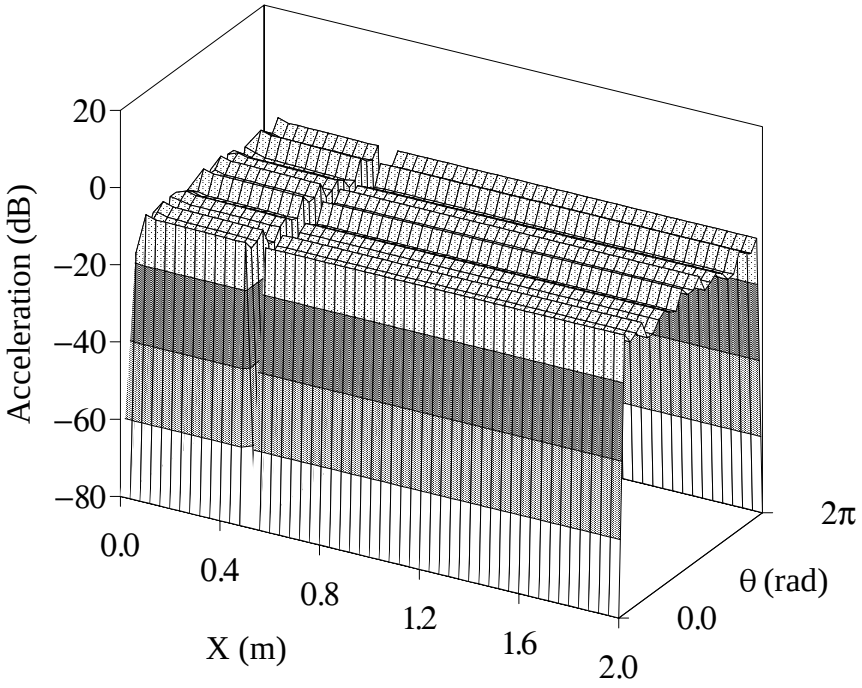

Figure 4.18 Uncontrolled semi-finite cylinder tangential acceleration distribution.

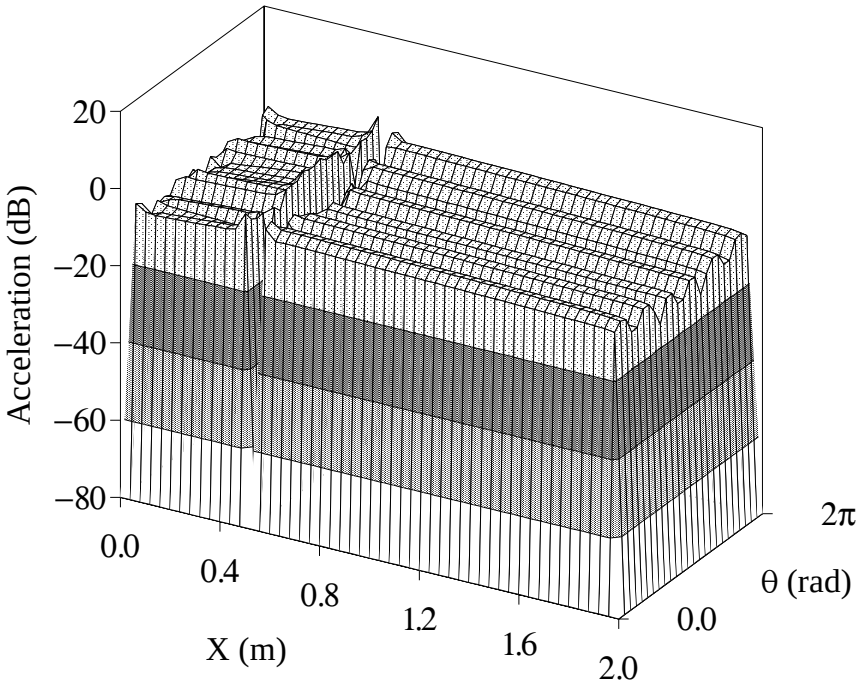

Figure 4.19 Uncontrolled finite cylinder tangential acceleration distribution.

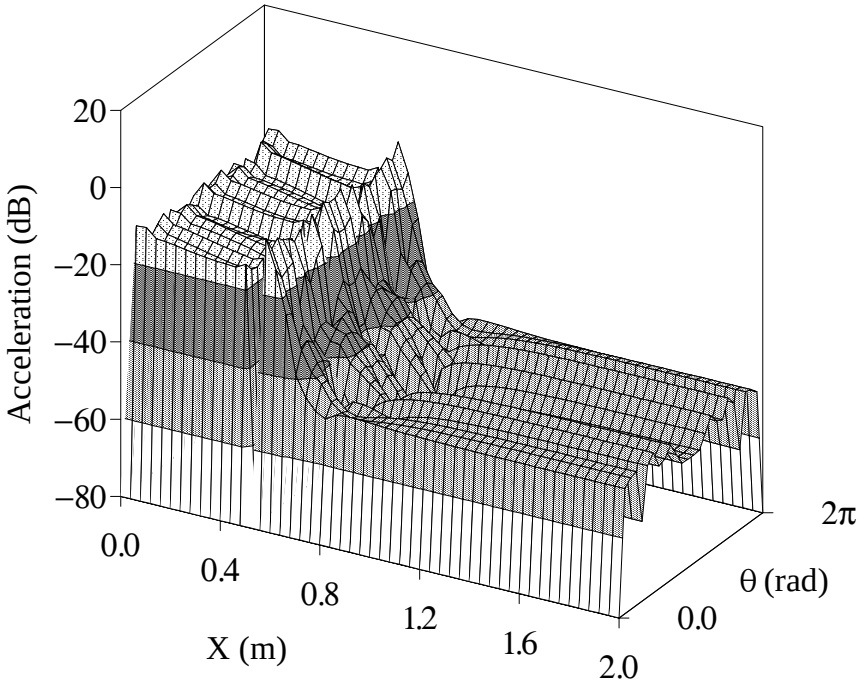

Figure 4.20 Controlled semi-finite cylinder tangential acceleration distribution - control sources driven independently.

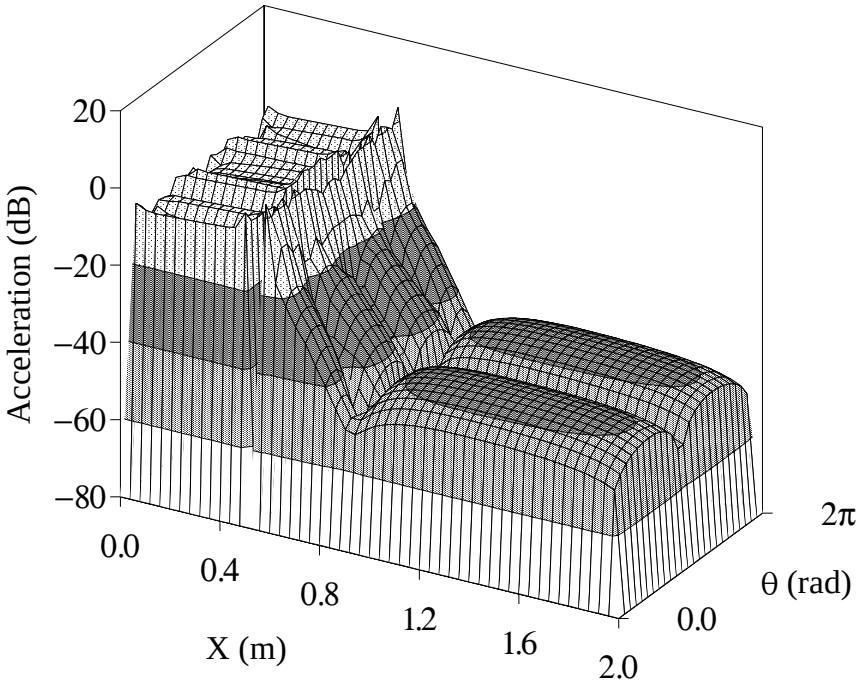

Figure 4.21 Controlled finite cylinder tangential acceleration distribution - control sources driven independently.

4.3.2 Effect of variations in forcing frequency, control source location and error sensor location on the control forces

Figure 4.22 shows the effect of varying the forcing frequency on the magnitude of the control force(s) required to minimise the radial cylinder vibration at the line of error sensors. The mean control source amplitudes for the cases where control sources are driven by the same signal are low and do not vary significantly with frequency. For the cases with control sources driven independently, the mean control source amplitude is larger, and varies a little with frequency, particularly for the finite cylinder case. The corresponding results for beam and plate structures show large maxima in the control source amplitudes that are a result of the control source location corresponding to a standing wave node; this situation does not arise for the cylinder structures where the bending wavelength greatly exceeds the cylinder length.

Figures 4.23 and 4.24 show the effect of the locations of the ring of control sources and the line of error sensors on the control source amplitude required for optimal control. There are fluctuations in the control effort required with different axial locations of control sources and error sensors, again particularly for the finite cylinder, but no large maxima in control effort occur.

These results show that, unlike for the equivalent beam and plate cases, there are no frequencies or axial locations of control sources and error sensors that result in an unrealistically high control effort required to optimally control the vibration at the ring of error sensors.

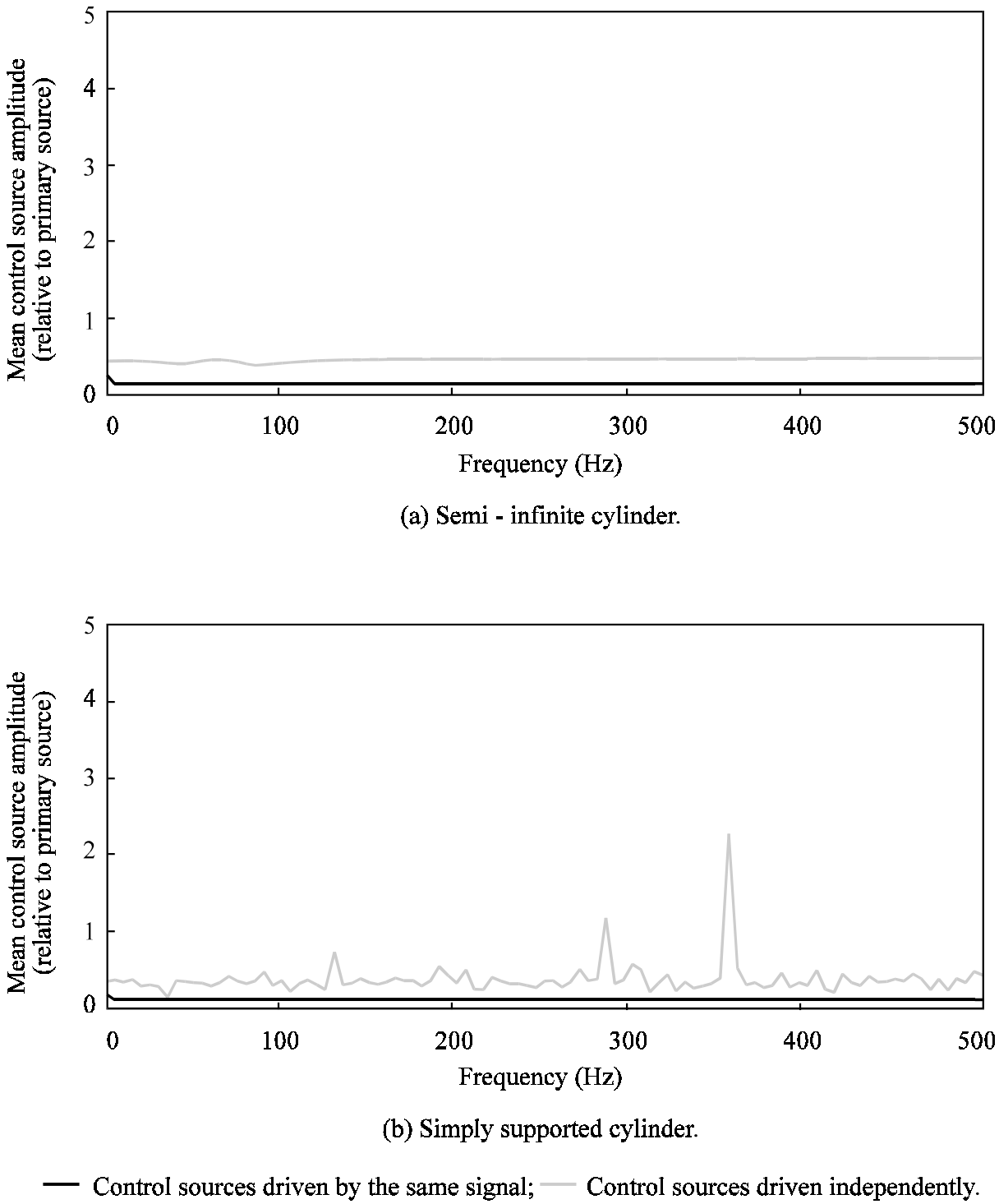

Figure 4.22 Mean control source amplitude for optimal control as a function of frequency. Six control sources and two primary sources were used.

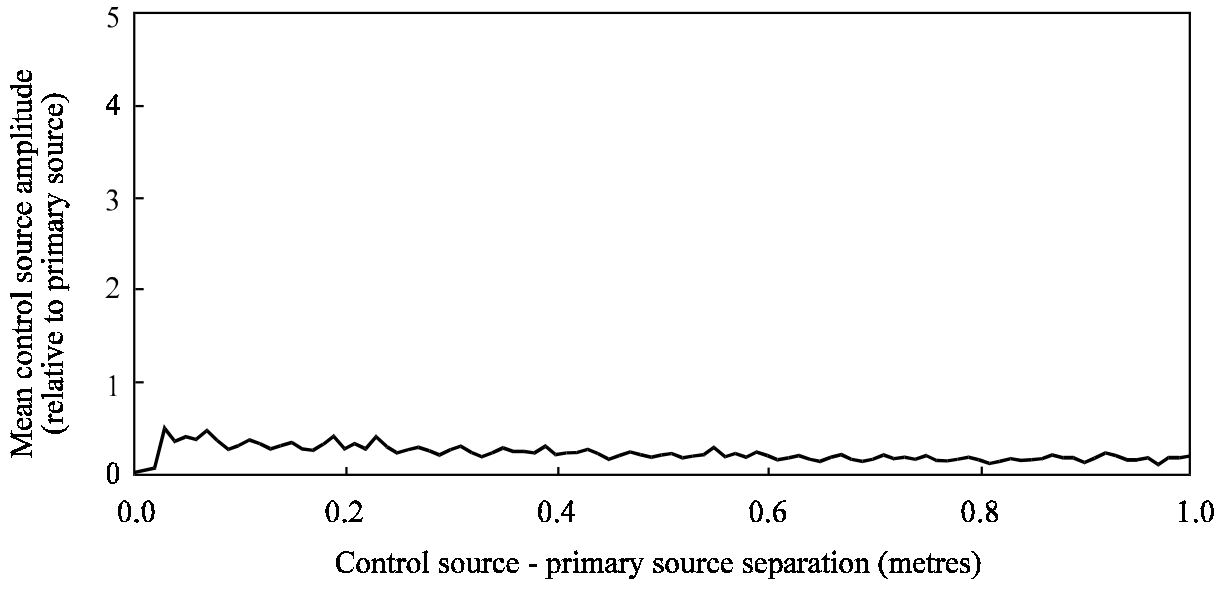

(a) Semi - infinite cylinder.

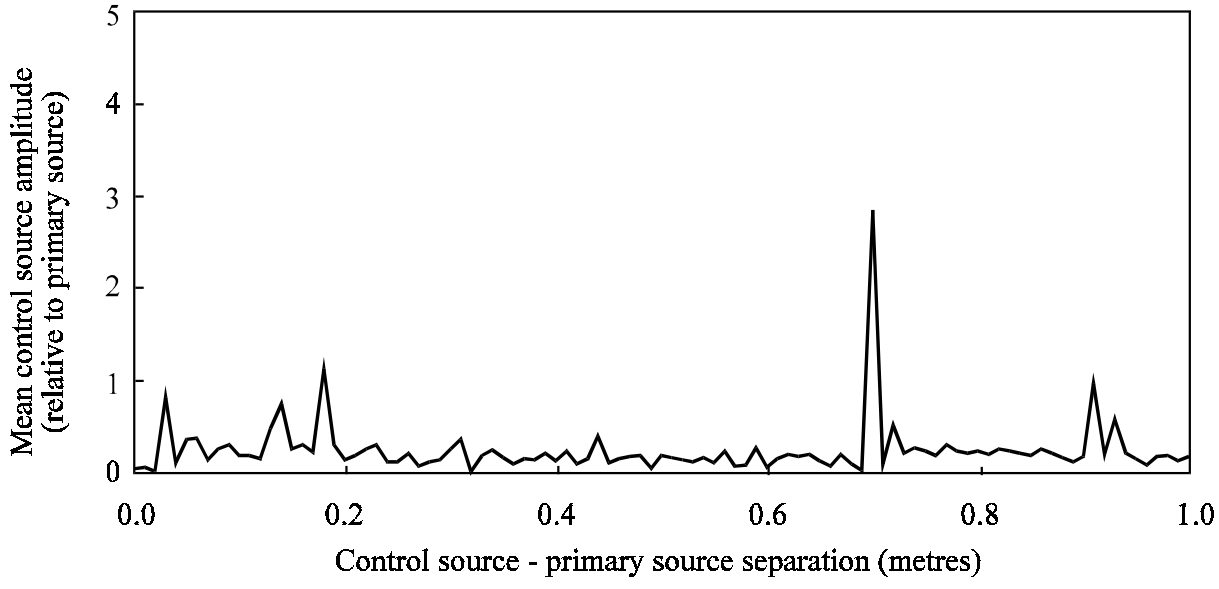

(b) Simply supported cylinder.

Figure 4.23 Mean control source amplitude for optimal control as a function of control source - primary source separation. Six control sources and two primary sources were used.

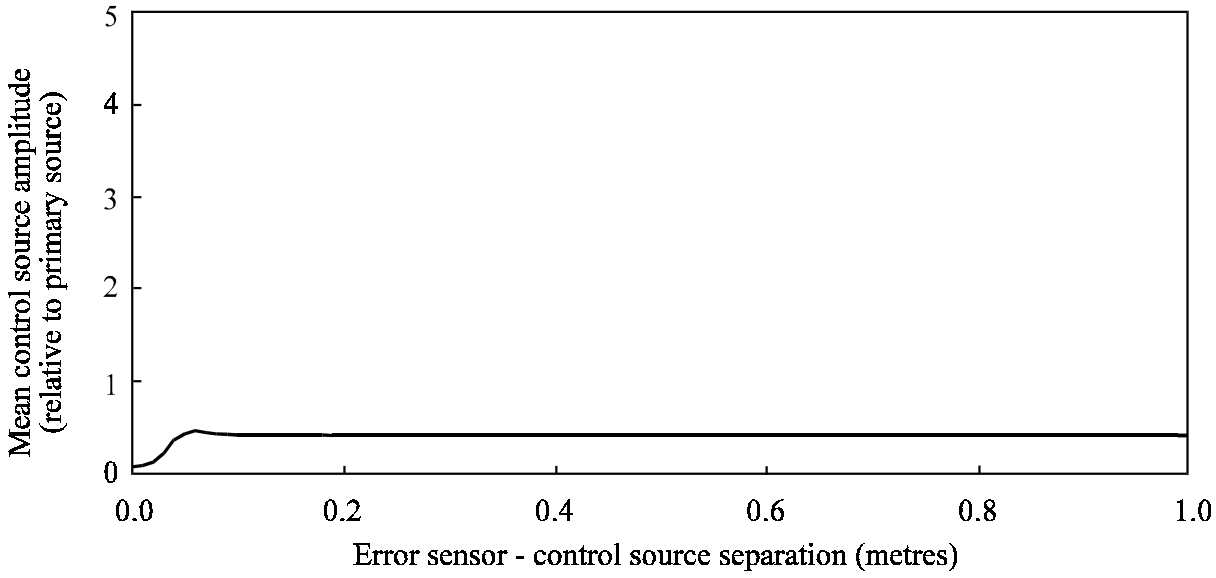

(a) Semi - infinite cylinder.

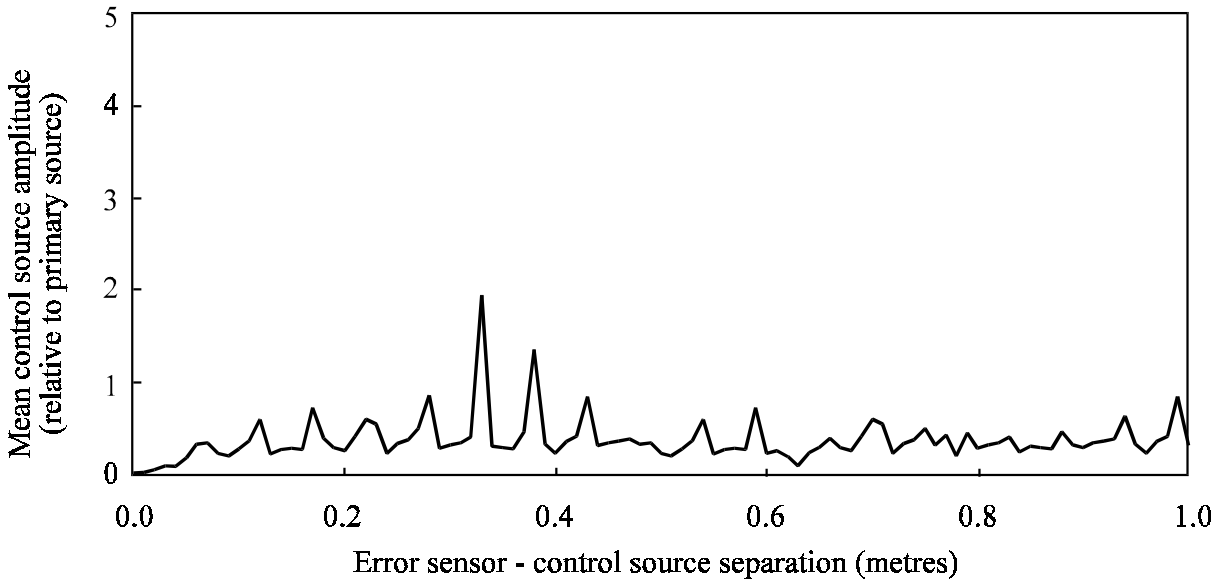

(b) Simply supported cylinder.

Figure 4.24 Mean control source amplitude for optimal control as a function of error sensor - control source separation. Six control sources and two primary sources were used.

Figure 4.25 shows the dependence of control source amplitude required for optimal control on circumferential control source location.

Figure 4.25(a) shows the amplitude of the second control source required for optimal control, assuming only two control sources are used, and the first is located at $\theta_{c1} = \pi/6$ radians. If the second control source is located near to the first, the control source amplitude required for optimal control tends toward infinity. This also occurs when the second control source is located near $\theta_{c2} = 2\pi - \theta_{c1} = 11\pi/6$.

Figure 4.25(b) shows the amplitude of the third control source required for optimal control, assuming three control sources are used. The first is located at $\theta_{c1} = \pi/6$ and the second at $\theta_{c2} = 3\pi/4$ radians. If the third control source is located near to either of the first two, the control source amplitude required for optimal control becomes large. This also occurs when the third control source is located near $\theta_{c3} = 2\pi - \theta_{c1} = 11\pi/6$ or $2\pi - \theta_{c2} = 5\pi/4$.

Figure 4.25(c) shows the amplitude of the fourth control source required for optimal control, assuming three control sources are used. The first is located at $\theta_{c1} = \pi/6$, the second at $\theta_{c2} = 3\pi/4$ and the third at $\theta_{c3} = 35\pi/24$ radians. If the fourth control source is located near to either of the first three, the control source amplitude required for optimal control becomes large. This also occurs when the fourth control source is located near $\theta_{c4} = 2\pi - \theta_{c1} = 11\pi/6$, $2\pi - \theta_{c2} = 5\pi/4$ or $2\pi - \theta_{c3} = 13\pi/24$.

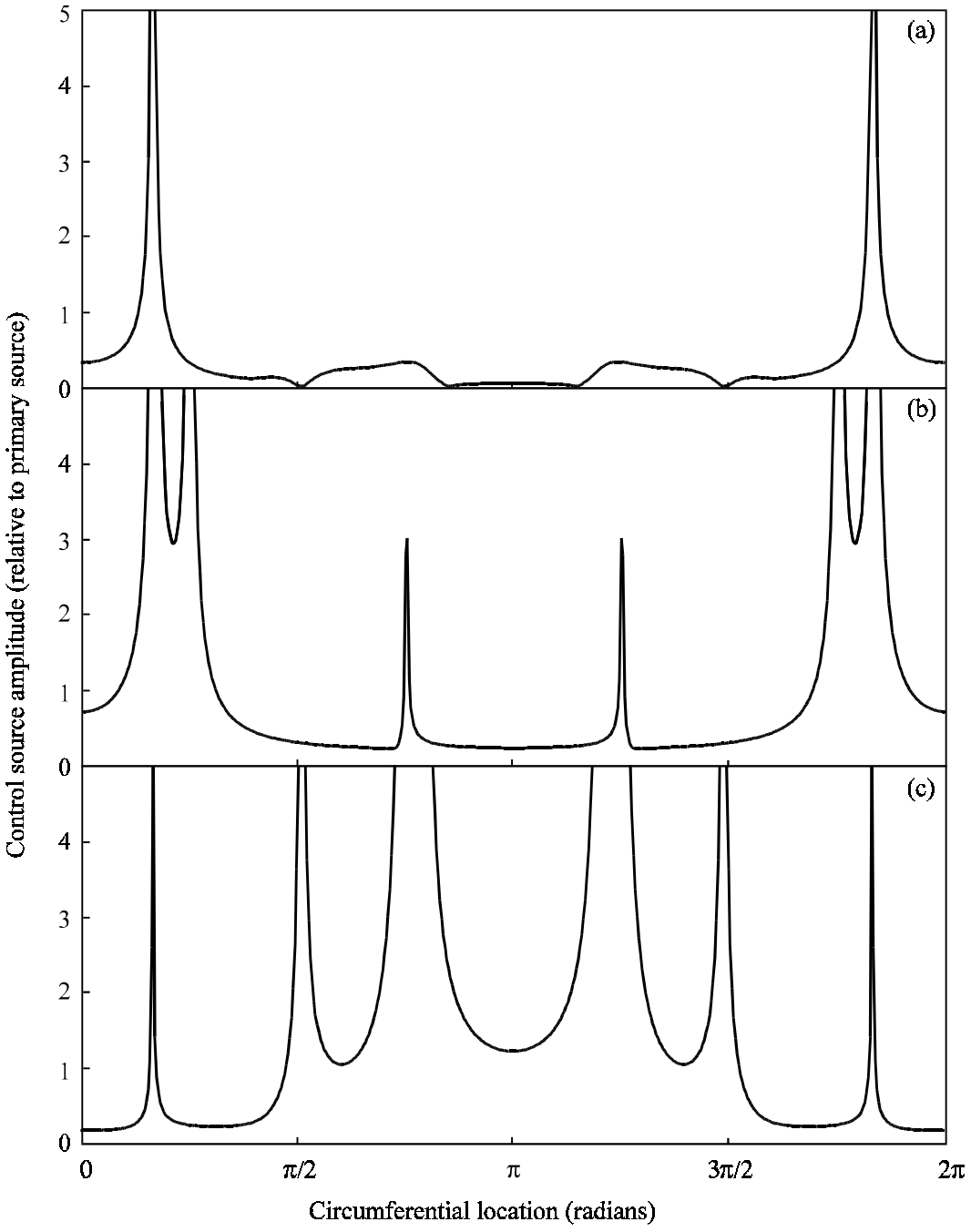

Figure 4.25 Control source amplitude for optimal control as a function of circumferential control source location.

(a) Amplitude of the second of two control sources; the first control source was located at $\theta_{c1} = \pi/6$ radians.

(b) Amplitude of the third of three control sources; the first control source was located at $\theta_{c1} = \pi/6$ and the second at.$\theta_{c2} = 3\pi/4$ radians.

(c) Amplitude of the fourth of four control sources; the first control source was located at $\theta_{c1} = \pi/6$, the second at $\theta_{c2} = 3\pi/4$ and the third at $\theta_{c3} = 35\pi/24$ radians.

If the circumferential location of an additional control source is θ_{i+1} and there are i control sources already in place at locations θ_i, then the amplitude of control source i+1 will be large when $\cos(\theta_{i+1}) = \cos(\theta_i)$, because at these locations, control source i+1 contributes to the same modes as one of the other control sources.

4.3.3 Effect of variations in forcing frequency, control source location and error sensor location on the attenuation of acceleration level

Figure 4.26 shows the variation in the mean attenuation of radial, axial and tangential acceleration level downstream of the ring of error sensors as a function of frequency for the cases with control sources driven independently. There is some variation, particularly for the semi-infinite cylinder below 200 Hz, but overall the amount of attenuation of acceleration in each direction is not greatly dependent on the excitation frequency. Radial acceleration is attenuated slightly more than axial and tangential acceleration, and axial acceleration is also attenuated slightly more than tangential acceleration.

Figure 4.27 shows that little attenuation can be achieved using control sources driven by a common signal. This is because there are many circumferential modes contributing significantly to the vibration of the cylinder, even at low frequencies. The level of attenuation achieved is not greatly dependent on the separation between control sources and primary sources, as indicated by Figure 4.28. Figure 4.29 shows that attenuation of acceleration level increases with increasing separation between control sources and error sensors. Very little attenuation is achieved with the error sensors located close to the control sources.

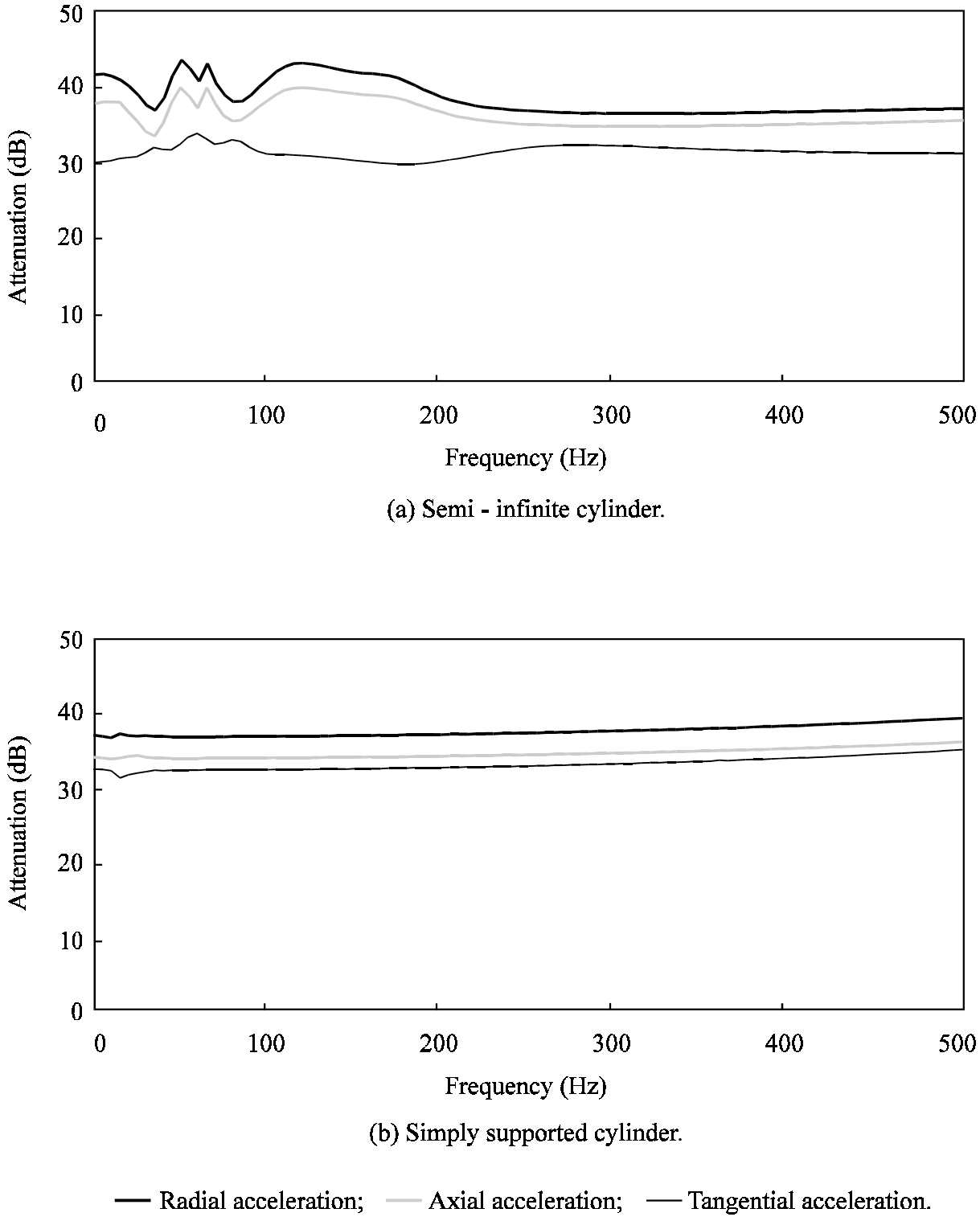

Figure 4.26 Mean attenuation downstream of the line of error sensors as a function of frequency, with the control actuators driven independently.

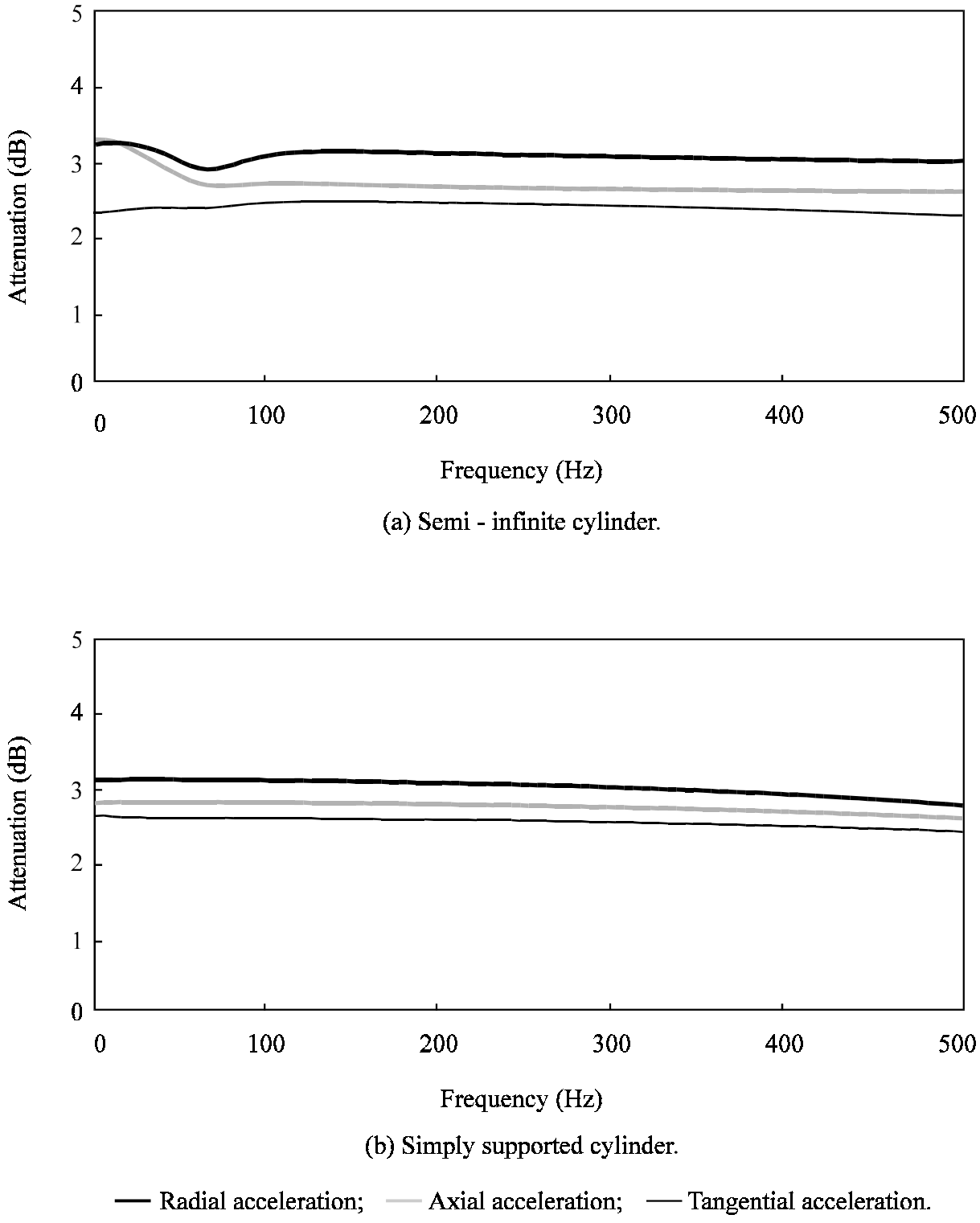

Figure 4.27 Mean attenuation downstream of the line of error sensors as a function of frequency, with the control actuators driven by the same signal.

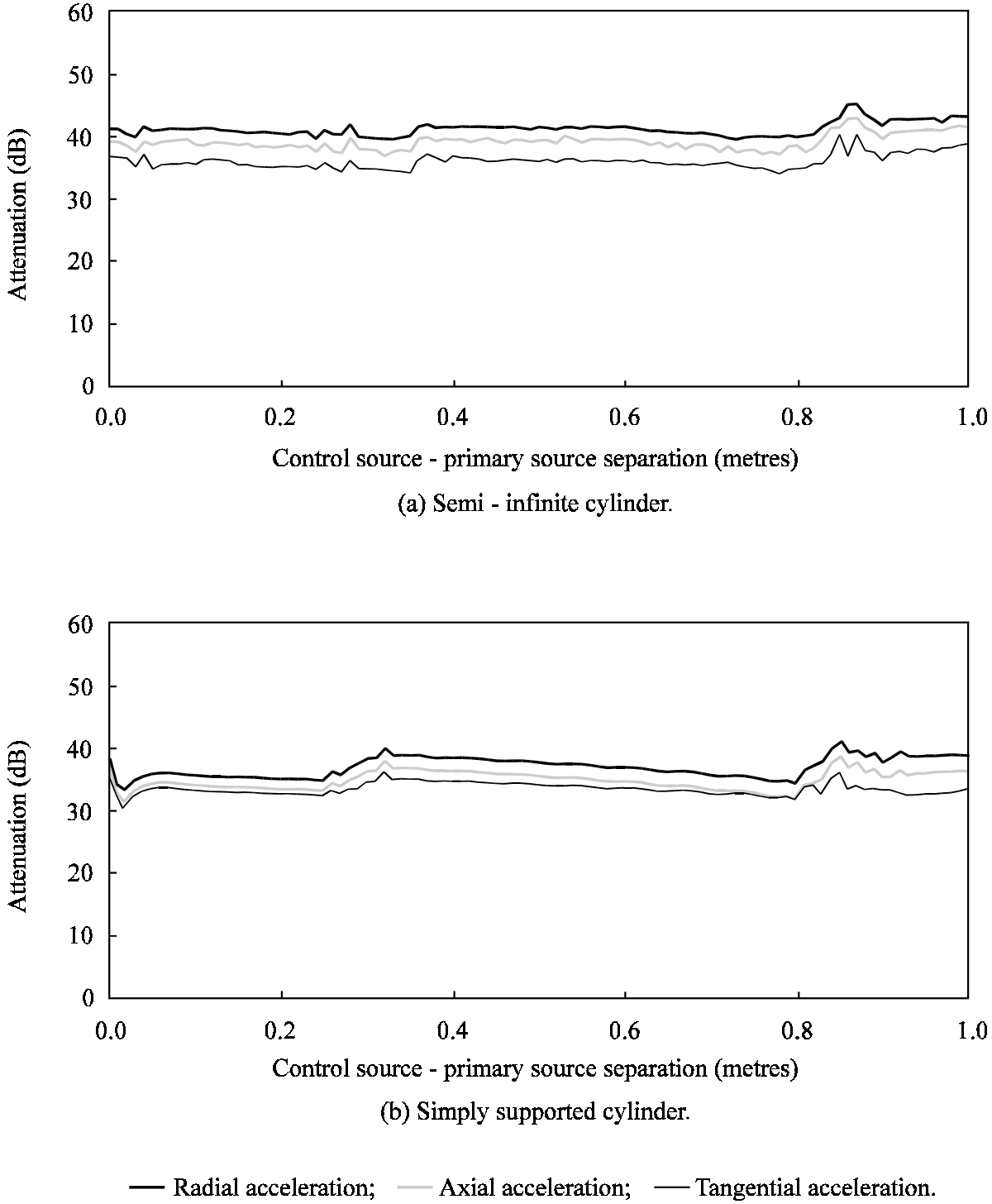

Figure 4.28 Mean attenuation downstream of the line of error sensors as a function of control source - primary source separation.

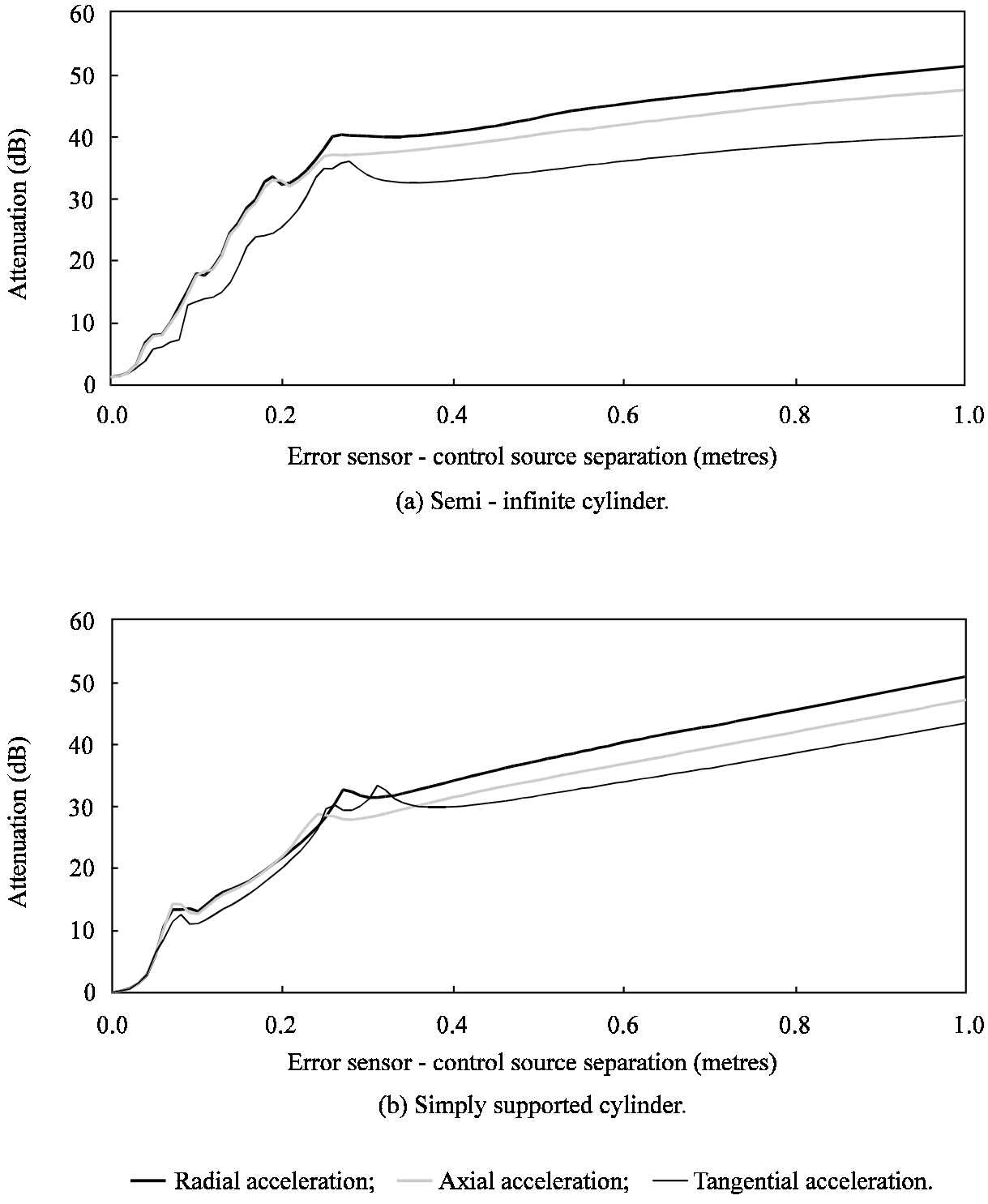

Figure 4.29 Mean attenuation downstream of the line of error sensors as a function of error sensor - control source separation.

4.3.4 Number of control sources required for optimal control

Table 4.3 shows the amount of attenuation of acceleration level achieved downstream of the error sensors with various numbers of control sources. The control sources are located at a single axial location. The locations of primary sources, control sources and error sensors and the cylinder dimensions used were those given in Table 4.1. The results given are for the simply supported cylinder.

Table 4.3

Effect of the Number of Control Sources on Mean Attenuation of Radial Acceleration

Number of Control Sources	Mean Attenuation (dB)
1	2.8225
2	10.883
3	35.902
4	36.976
5	36.976
6	36.976

4.3.5 Number of error sensors required for optimal control

Table 4.4 shows the control source amplitude and amount of attenuation of acceleration level achieved downstream of the error sensors with various numbers of error sensors. The error sensors were located at axial location x_e = 1.0m and unevenly spaced circumferential locations. The other locations of primary sources and control sources and the cylinder dimensions used were those given in Table 4.1. The results given are for the simply-supported cylinder.

Table 4.4

Effect of the Number of Error Sensors on Control Source Amplitude and Mean Attenuation

Number of Error Sensors	Mean Control Source Amplitude*	Mean Attenuation of Radial Acceleration (dB)	Mean Attenuation of Axial Acceleration (dB)	Mean Attenuation of Tangential Acceleration (dB)
1	0.14538	-0.62607	-0.93307	-082318
2	0.34850	8.0704	7.4881	6.8480
3	0.23683	36.035	32.944	32.050
4	0.24036	36.618	33.699	32.132
5	0.24036	36.619	33.700	32.131
6	0.24036	36.622	33.710	32.134
7	0.24036	36.626	33.713	32.137
8	0.24036	36.635	33.714	32.139
9	0.24036	36.644	33.721	32.141
10	0.24036	36.654	33.727	32.144
∞	0.24082	36.976	34.925	32.616

*Mean control source amplitude is expressed relative to the primary source amplitude. Six control sources and two primary sources were used.

4.3.6 Natural frequencies

Table 4.5 lists the natural frequencies of the cylinder described in Table 4.1, except that the effects of the ring stiffener have not been included. The experimental results of Section 4.5.1 indicate that the ring stiffener increases the natural frequencies of each mode by a small amount.

Table 4.5

Natural Frequencies of the Unstiffened Cylinder

Natural Frequency (Hz)		Axial Mode Number				
		1	2	3	4	5
Circumferential Mode Number	0	1331	1602	2408	3177	3252
	1	321	890	1480	1982	2363
	2	114	392	756	1133	1485
	3	106	222	429	680	946
	4	179	216	318	471	656
	5	284	299	342	425	540
	6	415	424	446	488	556
	7	571	578	592	618	659
	8	751	757	768	787	816

4.4 EXPERIMENTAL PROCEDURE

4.4.1 Modal analysis

A modal analysis was performed on the cylinder to be used in the vibration control experiment. The software package "PC Modal", a Brüel and Kjær type 8202 impact hammer and type 2032 signal analyser were used in the modal analysis. The modal analysis experimental arrangement is illustrated in Figure 4.30. The dimensions of the cylinder were the same as those given in Section 4.3 (see Table 4.1). The cylinder model consisted of 45 nodes dividing the cylinder into a line of 21 nodes parallel to the *x*-axis and a ring of 25 nodes parallel to the θ-axis. The analysis was performed for the two cases with and without the angle stiffener attached to the cylinder.

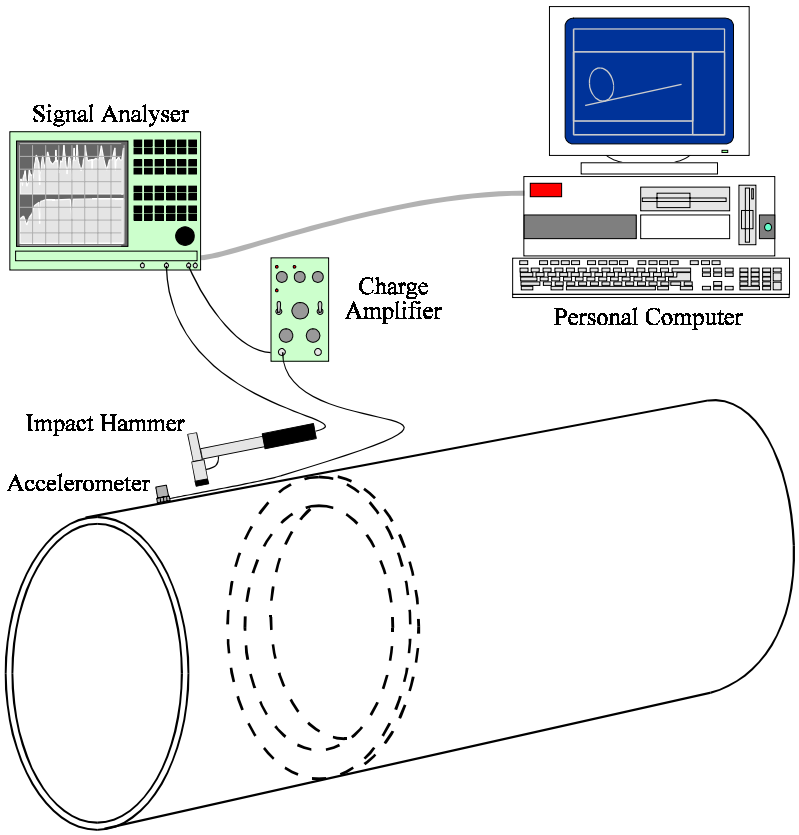

Figure 4.30 Experimental arrangement for the modal analysis of the cylinder.

4.4.2 Active vibration control

A steel stiffener was bolted tightly to a cylinder described by the dimensions given in Table 4.1. Six piezoceramic actuators were placed between the stiffener flange and the cylinder wall. The actuators were attached only at one end to ensure that no external tensile force were applied to them, as the type of actuator used is weak in tension. The primary source, control source and error sensor locations and the excitation frequency are given in Table 4.1.

The complete experimental arrangement is shown in Figure 4.31. The primary signal was produced by a signal analyser and amplified to drive the electrodynamic shakers (Figure 4.32). The shakers acted on the shell through force transducers, and the magnitudes of the primary forces were recorded using an oscilloscope.

The error signals from the ring of eight accelerometers (Figure 4.33) were passed to an EZ-ANC controller. The controller determined the control signals to drive the piezoceramic actuators, optimally minimising the acceleration measured by the error sensors. The control signals were also monitored on an oscilloscope.

The acceleration was measured at 10 or 15 cm intervals along the cylinder in four lines at locations $\theta = 0$, $\pi/6$, $\pi/4$ and $\pi/2$ (Figure 4.34). The accelerometer signals were read in turn through a 40 channel multiplexer connected to a Hewlett-Packard type 35665A signal analyser, in which the frequency response function was used to analyse the data. The magnitude and phase of the acceleration were recorded on a personal computer, which was also used to switch the

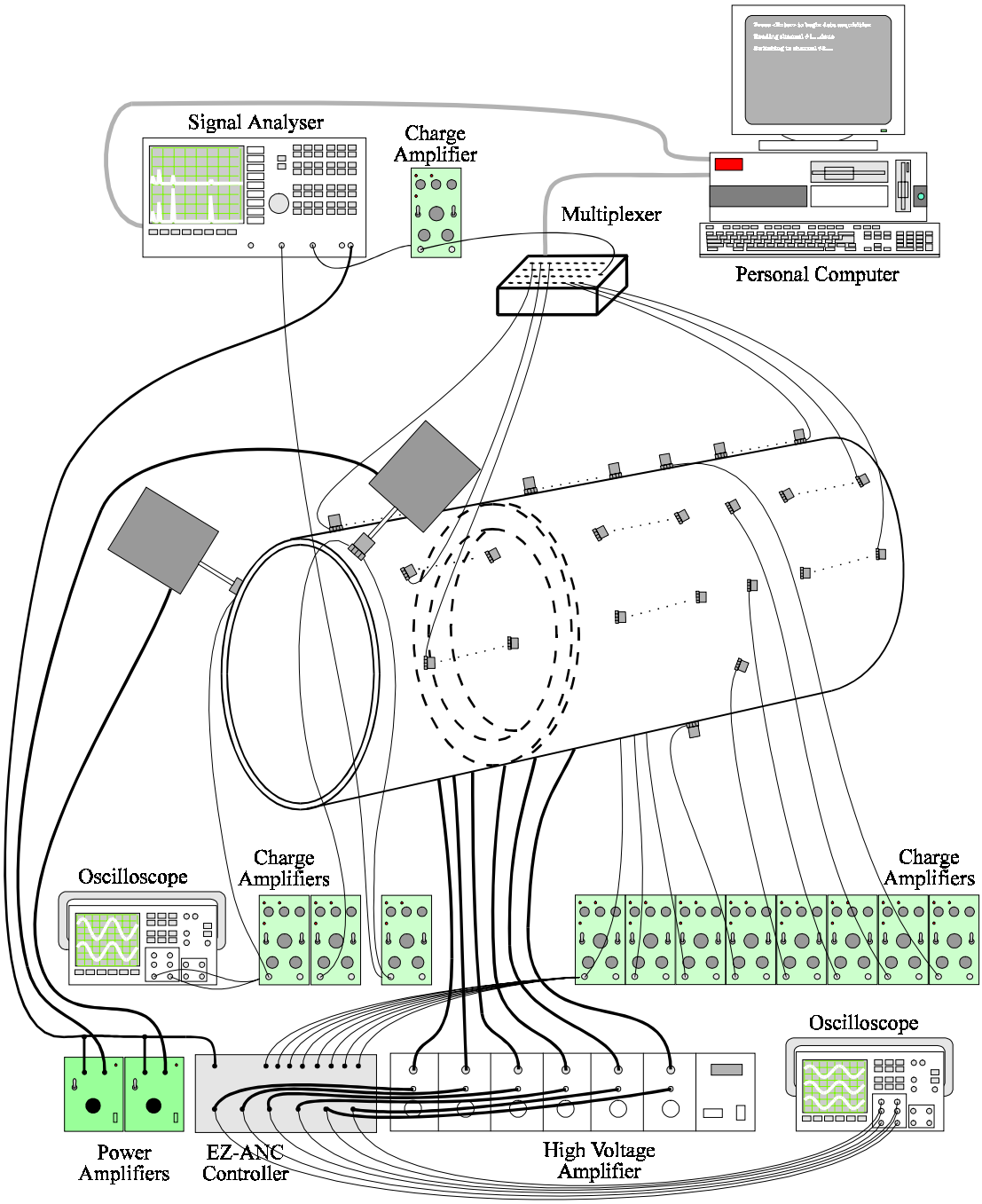

Figure 4.31 Experimental arrangement for the active control of vibration in the cylinder.

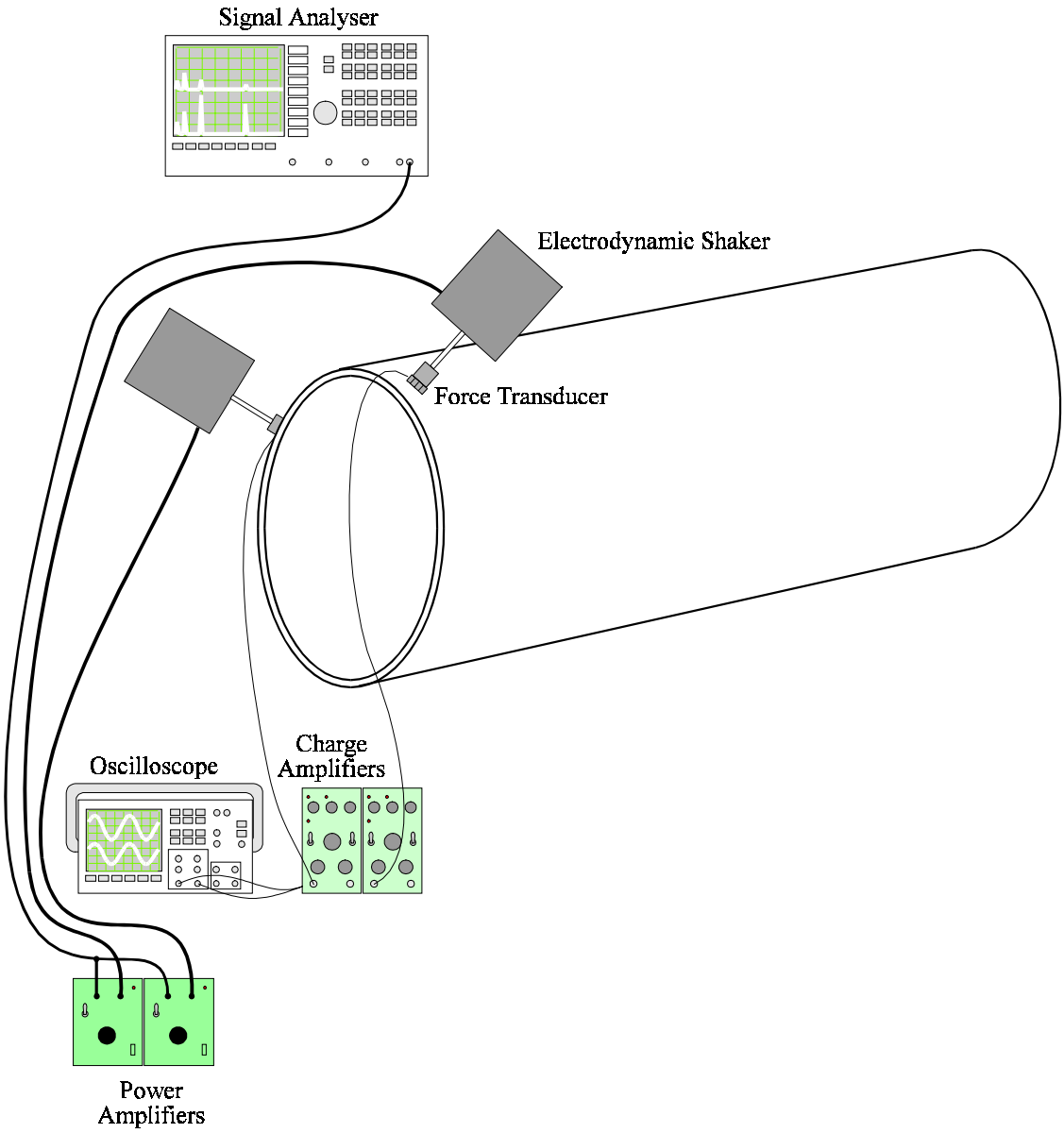

Figure 4.32 Primary system.

recorded channel on the multiplexer. The acceleration output of the force transducer at one of the primary source locations was used as the reference signal for the frequency response analysis. Accelerometer readings were taken initially once the error sensor signals had been optimally reduced, and again with the control amplifiers switched off (the uncontrolled case). The

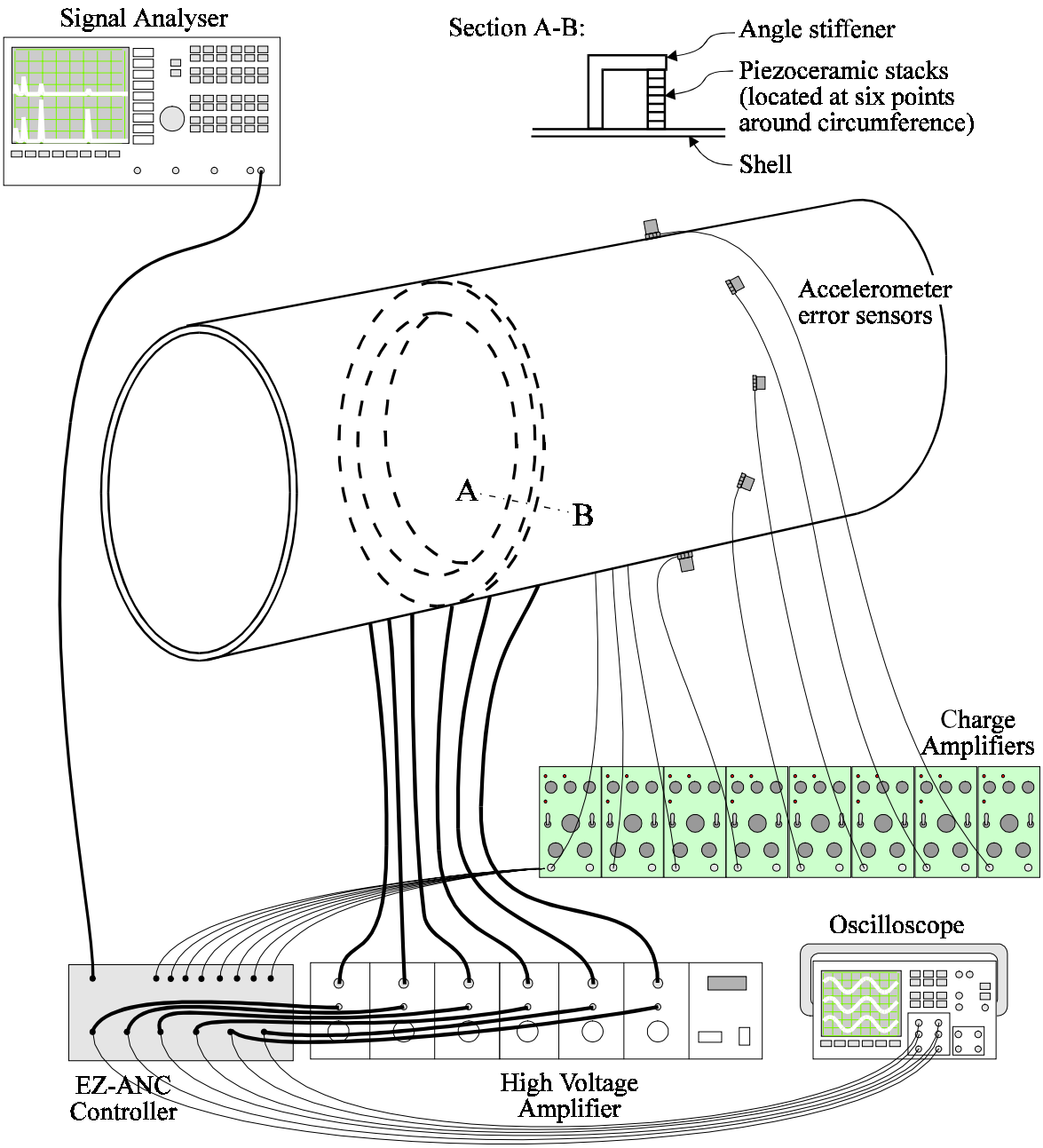

Figure 4.33 Control system.

experiment was repeated with the six control actuators driven by a common control signal.

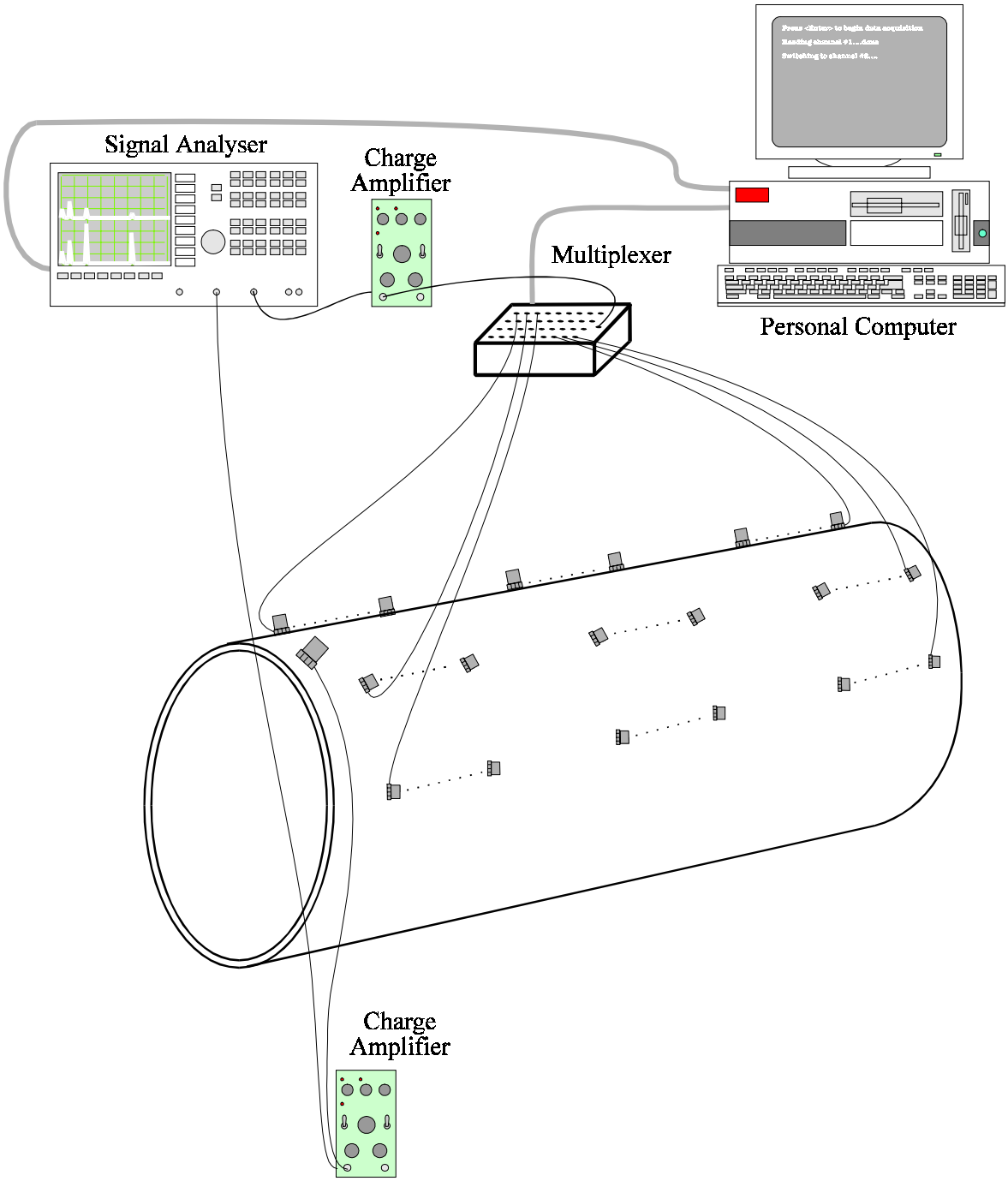

Figure 4.34 Acceleration measurement. Not all of the accelerometer - multiplexer connections are shown.

Figures 4.35 - 4.38 show the photographs of the experimental equipment. In Figure 4.35, the cylinder is shown with the signal generating and recording equipment around it. The cylinder is simply supported at each end. The two electromagnetic shaker primary sources can be seen. The accelerometers mounted on the cylinder are shown in Figure 4.36. The ring stiffener can be seen through the open end of the cylinder in Figure 4.37, which also shows the EZ-ANC controllers. The piezoceramic stack actuators are shown in Figure 4.38, mounted at various angles θ as described earlier in this section.

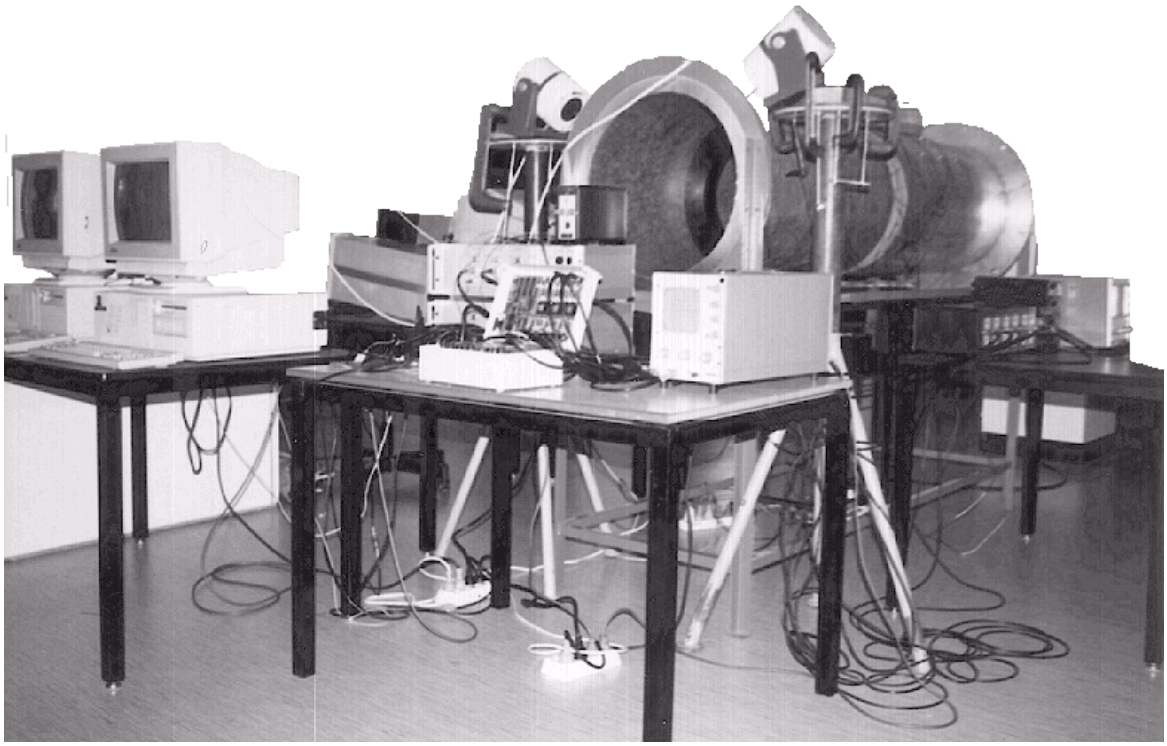

Figure 4.35 Experimental equipment for the active vibration control of cylinder vibration.

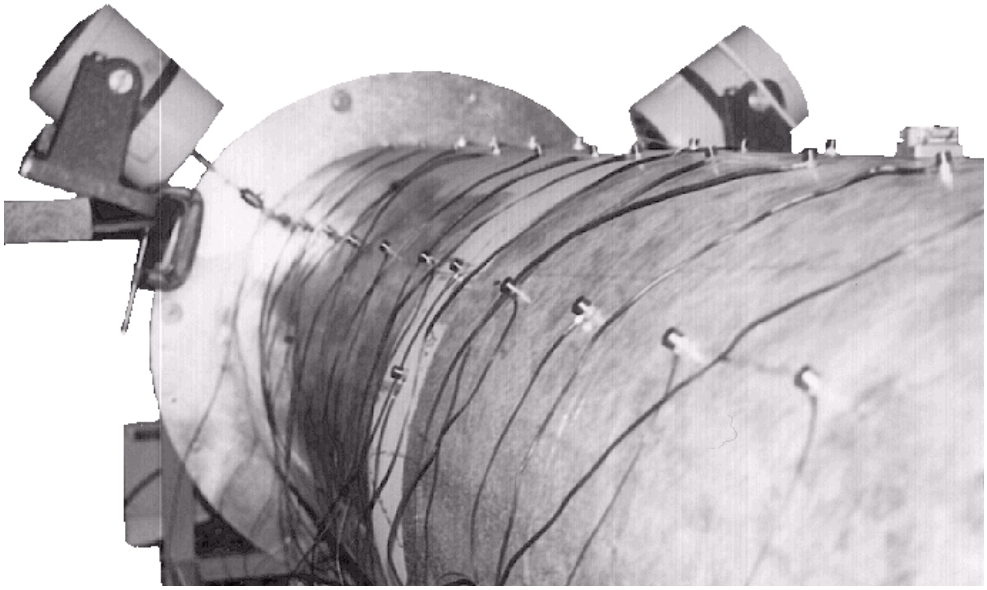

Figure 4.36 Accelerometers mounted on the cylinder.

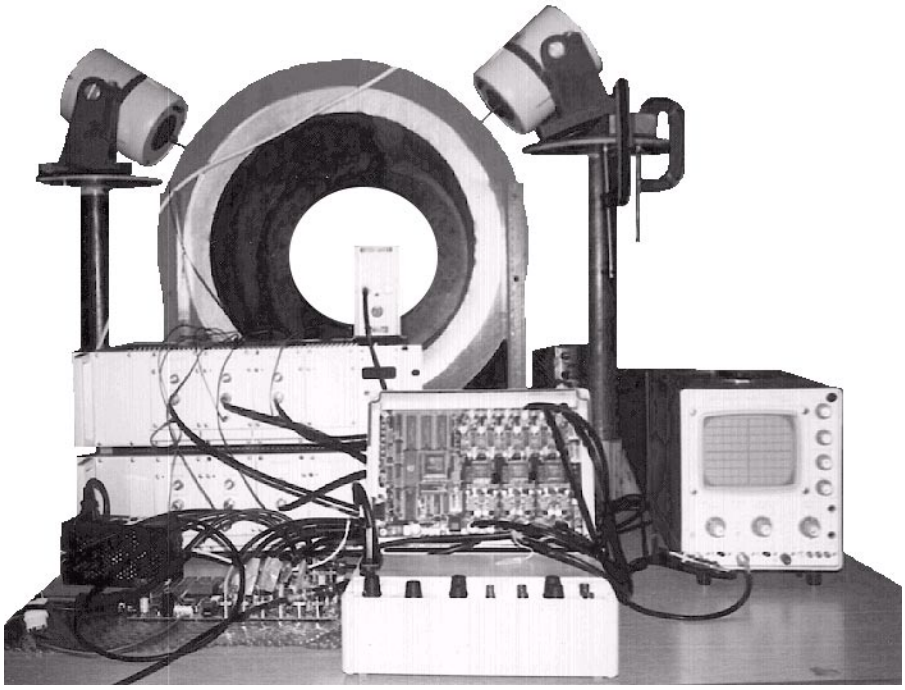

Figure 4.37 EZ-ANC controllers and control source amplifiers (foreground) with cylinder showing ring stiffener.

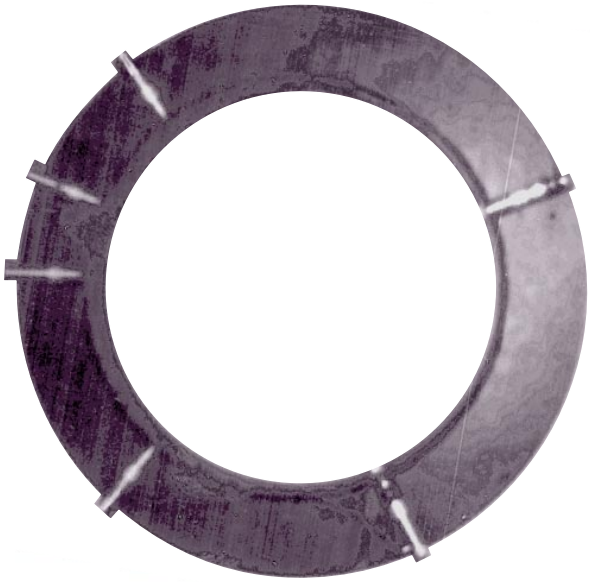

Figure 4.38 Piezoceramic stack actuators and the ring stiffener.

4.5 EXPERIMENTAL RESULTS

4.5.1 Modal analysis

The following figures show the modal analysis results. Each figure represents one ring around the circumference of the cylinder (located at x = 0.2m) and one line along the cylinder.

Figures 4.39 and 4.40 show the n,1 (n = 2,3,4,5) modes of vibration of the cylinder without the angle stiffener. These modes were significant on the unstiffened cylinder, but were not found to be significant modes for the cylinder with the ring-stiffener in place. Figures 4.41 - 4.43 compare the 5,2, 6,2 and 7,3 modes for the unstiffened and stiffened cylinder. The presence of the ring-stiffener greatly reduced the vibration amplitude of these modes also. However, the presence of the ring-stiffener did not significantly affect the n,4 modes (Figures 4.44 and 4.45), presumably because the stiffener was located at ¼ the length of the cylinder from one end, which is the location of a node in an n,4 vibration mode. The assumption that the cylinder displacement was limited at the stiffener location is borne out by these results.

It is also of interest that the higher order circumferential modes (n,5, n,6, n,7) are a significant part of the vibration response of the cylinder, as predicted by the theoretical model. The natural frequencies of the unstiffened cylinder also agree closely with the theoretical predictions (see Section 4.3.6).

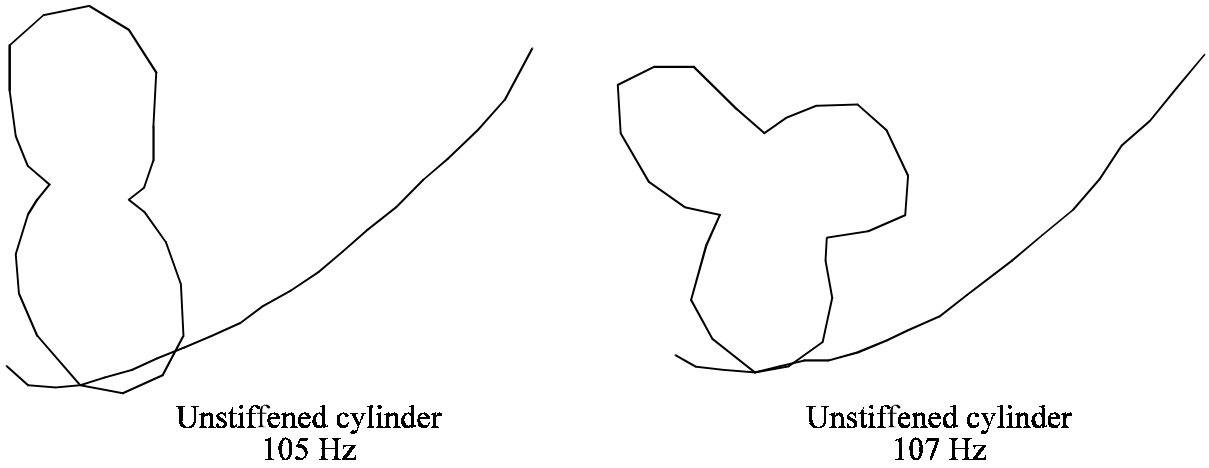

Figure 4.39 The 2,1 and 3,1 modes for the unstiffened cylinder.

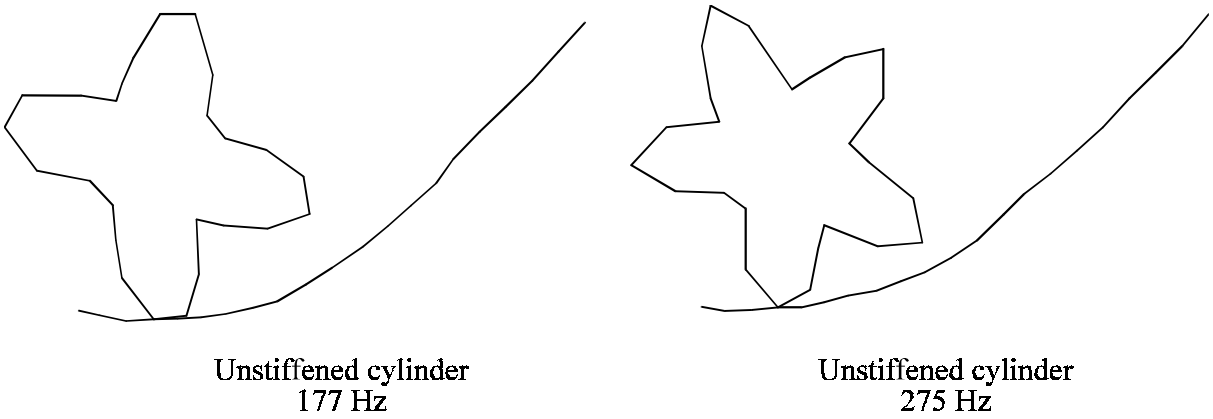

Figure 4.40 The 4,1 and 5,1 modes for the unstiffened cylinder.

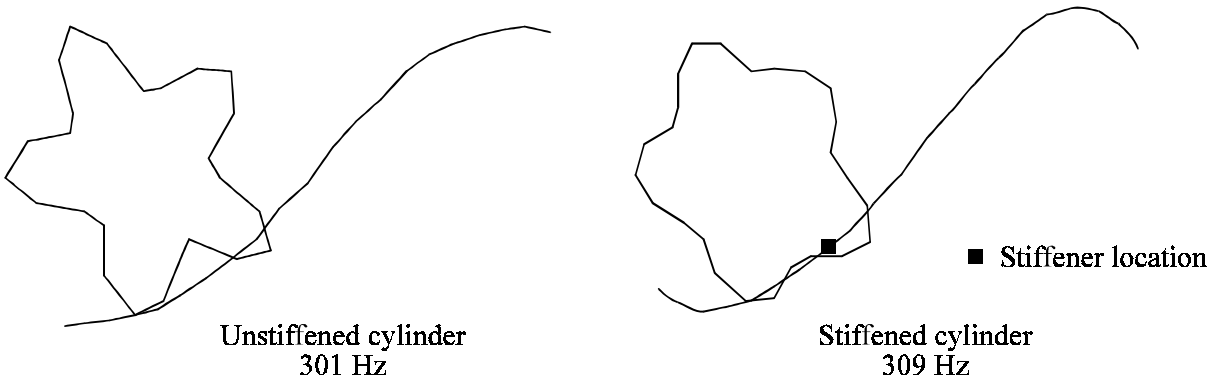

Figure 4.41 The 5,2 mode for the unstiffened and stiffened cylinder.

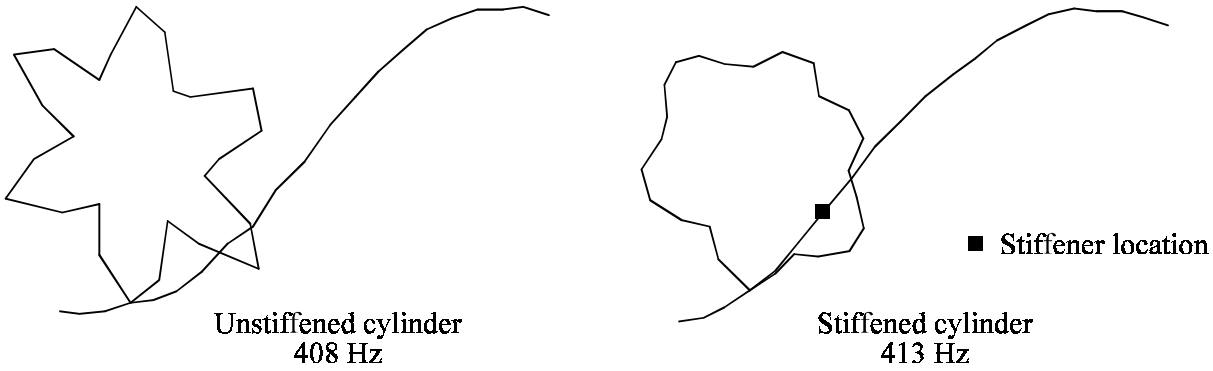

Figure 4.42 The 6,2 mode for the unstiffened and stiffened cylinder.

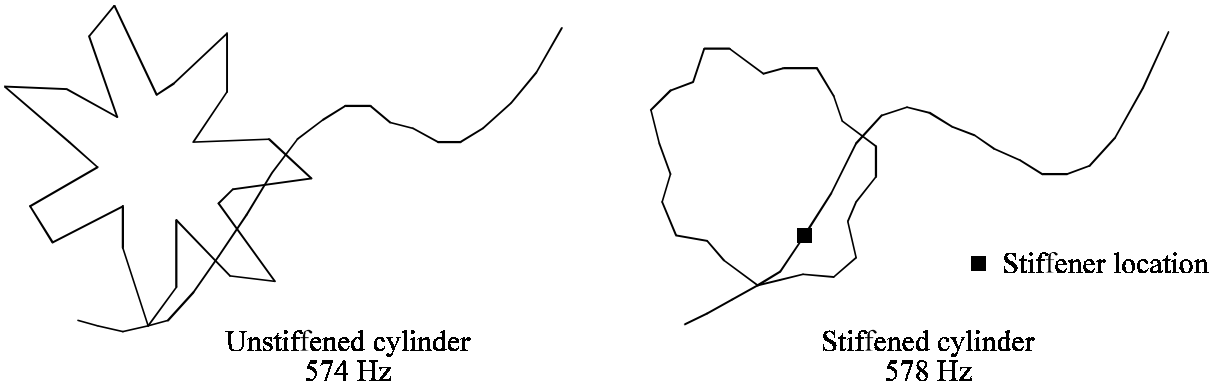

Figure 4.43 The 7,3 mode for the unstiffened and stiffened cylinder.

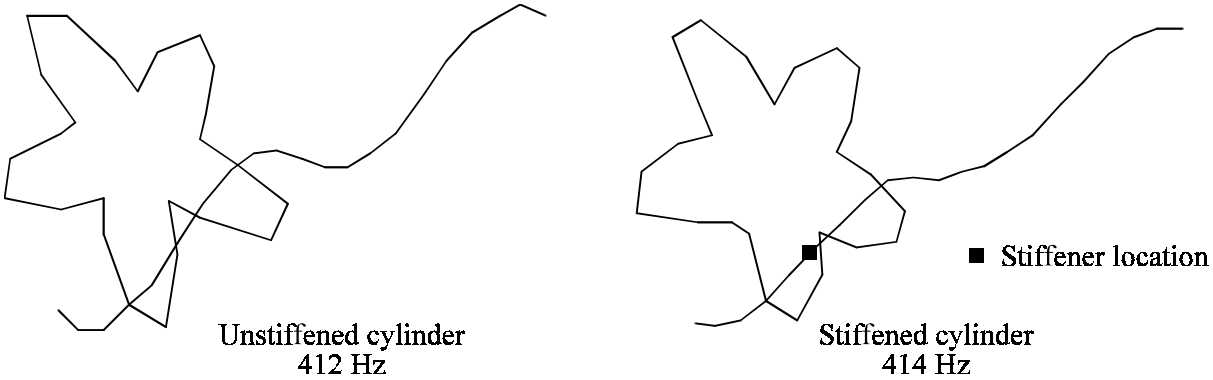

Figure 4.44 The 5,4 mode for the unstiffened and stiffened cylinder.

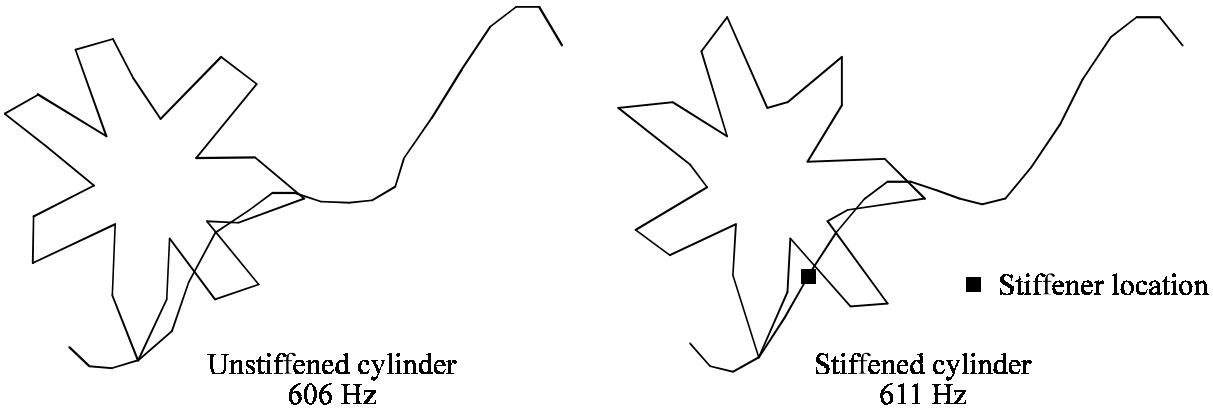

Figure 4.45 The 7,4 mode for the unstiffened and stiffened cylinder.

4.5.2 Active vibration control

Figure 4.46 shows the theoretical and experimental acceleration distributions for each of the four lines where accelerometers were placed in the experiment. For both the uncontrolled case and the controlled case with control actuators driven by the same signal, the experimental results and theoretical curves are in close agreement. For the controlled case with independently driven control sources, the theoretical analysis predicts greater reduction in acceleration level than was achieved experimentally. An error analysis showed that a very small error (0.12%) in the control signal would produce a decrease in attenuation corresponding to the difference between the experimental and theoretical data.

Table 4.6 compares the acceleration levels of radial, axial and tangential acceleration measured at four points on the cylinder both without and with active vibration control. The measurements were made using tri-axial accelerometers. The table shows that axial and tangential acceleration

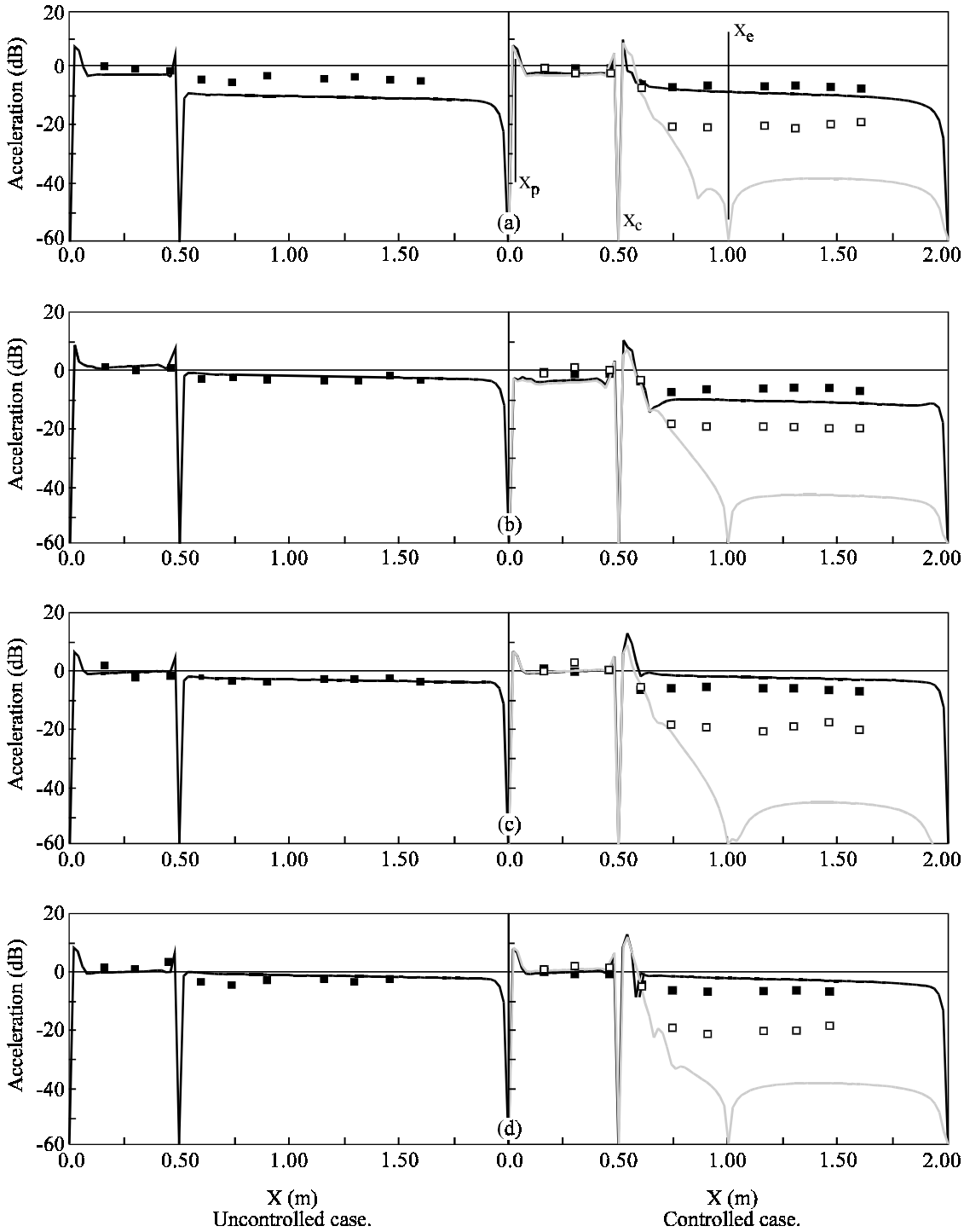

(1) Uncontrolled case; (2) Controlled case. —— Theoretical results and ▪ experimental data for the case with three control sources driven by the same signal; —— Theoretical results and ▫ experimental data for the case with independently driven control sources.
(a) $\theta = \pi/6^c$; (b) $\theta = 11\pi/24^c$; (c) $\theta = 7\pi/12^c$; (d) $\theta = 3\pi/4^c$.
x_p = primary source location; x_c = control source location; x_e = error sensor location.

Figure 4.46 Experimental acceleration distributions.

Table 4.6

Acceleration Levels of Radial, Axial and Tangential Acceleration

	Measurement Location		Radial Acceleration Level (dB)	Axial Acceleration Level (dB)	Tangential Acceleration Level (dB)
	x (m)	θ (rad)			
Uncontrolled	0.2	π/6	-0.8	-1.2	-6.8
	0.2	π/3	1.1	0.4	-1.1
	1.8	π/6	-7.2	-7.7	-13.4
	1.8	π/3	-6.8	-7.4	-7.7
Controlled	0.2	π/6	-0.9*	0.2*	-4.2*
	0.2	π/3	-0.7*	-0.3*	-2.6*
	1.8	π/6	-20.6	-20.6	-22.5
	1.8	π/3	-21.9	-22.4	-23.7

*These values are measurements from upstream of the control location.

are significantly reduced by minimising radial acceleration at the ring of error sensors.

The measurements taken at $\theta = \pi/6$ radians support the theoretical finding that nodes in the tangential vibration occur at opposite circumferential locations to nodes in axial and radial vibration. At $\theta = \pi/6$, the tangential acceleration level is several dB less than the levels recorded for axial and radial acceleration, while the levels are similar at the other circumferential location recorded.

4.6 SUMMARY

A theoretical model has been developed to describe the vibration response of a ring-stiffened cylinder to a range of excitation types, and in particular to describe the vibration response of ring-stiffened cylinders to point force primary excitation sources and angle stiffener and piezoceramic stack control sources. The numerical results indicate that flexural vibrations in cylinders can be actively controlled using piezoceramic stack actuators placed between the flange of an angle stiffener and the cylinder surface. Numerical results also indicate:

(1) Vibration in the axial, tangential and radial directions is coupled, and vibration amplitudes in each direction are of a similar order of magnitude for the cylinders considered.

(2) Circumferential modes in the axial and radial vibration standing waves occur at the same circumferential locations on the cylinder while modes of tangential vibration are located out-of-phase relative to the axial and radial modes.

(3) Optimally controlling radial vibration also significantly reduces axial and tangential vibration levels.

(4) The mean amplitude of the control forces required for optimal control is not greatly dependent on frequency, axial control source location or axial error sensor location. There are minor fluctuations, particularly for the finite cylinder, but no pattern or

increasing or decreasing trends.

(5) The optimum control forces are either in phase or 180^{o} out of phase with the primary sources. This is true for the semi-infinite cylinder as well as the finite cylinder, because a standing wave is generated by the vibration reflections from the finite end and the angle stiffener.

(6) Increasing the separation between the primary and control sources does not greatly affect the mean attenuation of acceleration level downstream of the ring of error sensors.

(7) Increasing the separation between the error sensors and the control sources significantly improves the mean attenuation of acceleration level downstream of the ring of error sensors.

(8) Because of the distance between nodes in axial standing waves in the cylinders considered, there are no axial locations of control sources and error sensors that give maxima in control source amplitude or minima in attenuation.

(9) Little or no reduction is achieved with control sources driven by a common control signal, because higher order circumferential modes of vibration contribute significantly to the vibration response of the cylinder even at low frequencies.

(10) The circumferential location of the control sources is significant. Generally, for every control source, there are two locations at which placement of an additional control source will require excessive control source amplitudes for optimal control.

(11) For the cylinder and frequency considered, optimal attenuation can be achieved with four control sources and four error sensors. Attenuation is only a little less with three control sources and three error sensors, but very little control is achieved with two or less control sources and error sensors.

The theoretical model outlined was verified experimentally for the cylinder with simply supported ends. A modal analysis of the cylinder indicated that the angle stiffener made a significant difference to the vibration response of the cylinder and that higher order circumferential modes contributed significantly to the overall response. Comparison between experimental results and theoretical predictions for the vibration of the cylinder with and without active vibration control showed that:

(1) The theoretical model accurately predicted the vibration response of the cylinder for the uncontrolled case and the case with control sources driven by the same signal.

(2) The theoretical model predicted more attenuation than could be achieved experimentally for the case with independently driven control sources. An error analysis indicated that an error in the control source signal of 0.12% would produce a decrease in attenuation

corresponding to the difference between the theoretical prediction and the experimental result. Nevertheless, around 18 dB attenuation was achieved experimentally for the case with independently driven control sources.

(3) Experimental measurements of axial and tangential vibration were of similar order to measurements of radial vibration, as predicted by the theoretical model. Axial and tangential vibration was significantly reduced as well as radial vibration when radial vibration was used as the error function.